# Material Matters™

VOLUME 14 • NUMBER 4

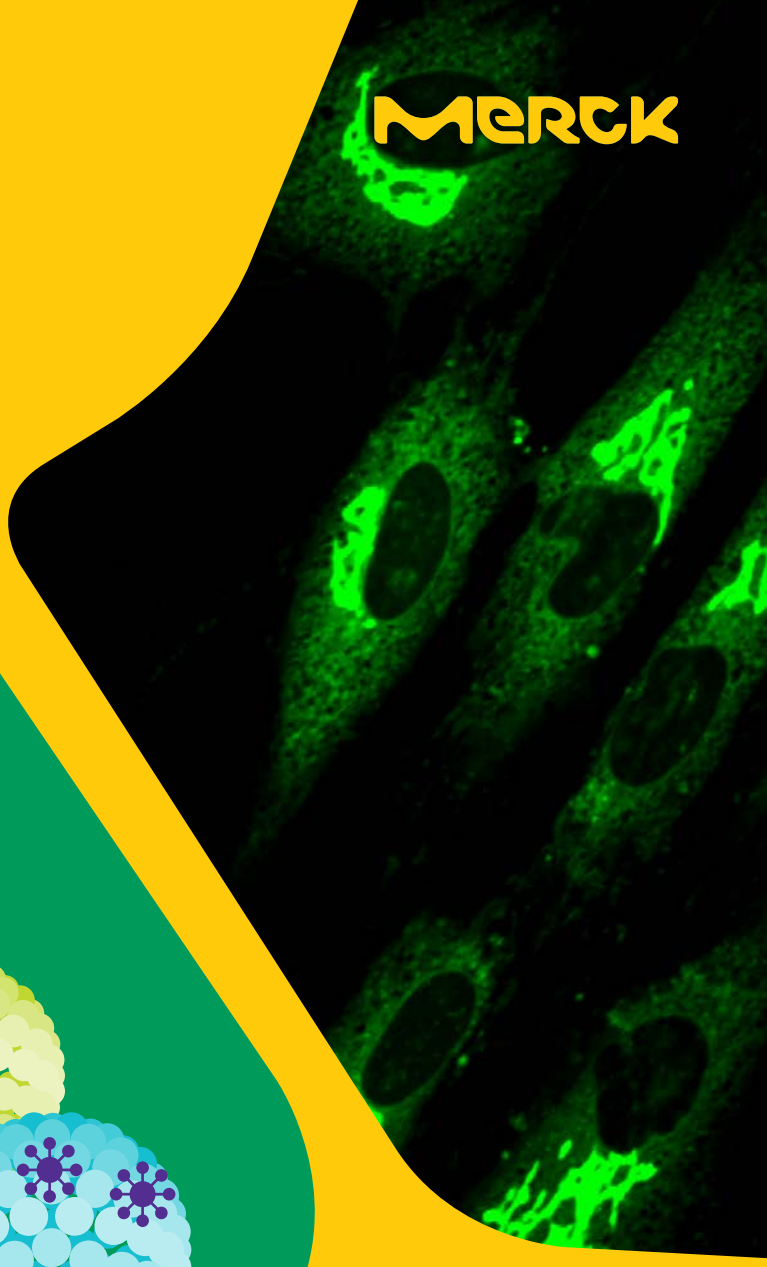

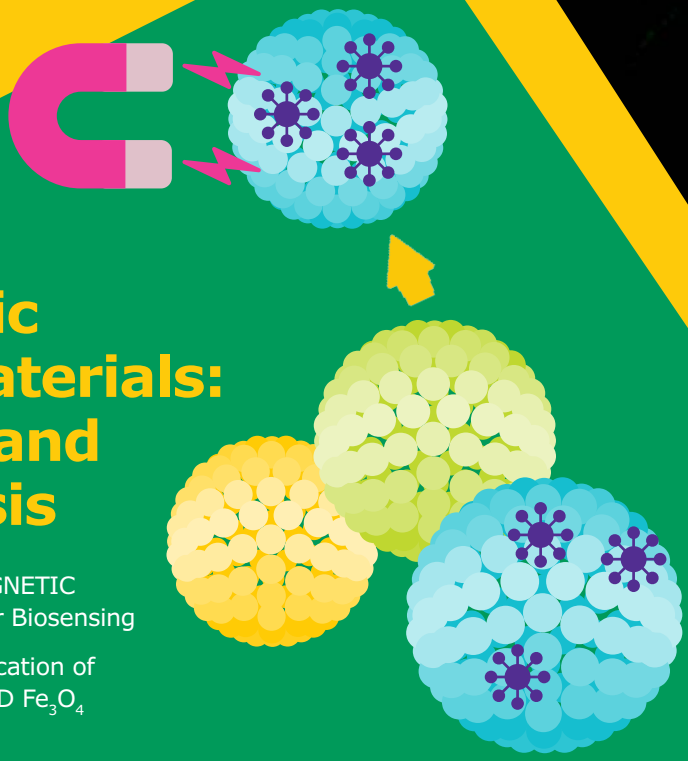

## Magnetic Nanomaterials: Design and Synthesis

SYNTHESIS OF MAGNETIC NANOPARTICLES for Biosensing

Synthesis and Application of SHAPE-CONTROLLED $Fe_3O_4$ NANOSTRUCTURES

MAGNETIC-PLASMONIC HYBRID NANOBEADS Designed for Imaging and Isolation of Cellular Organelles

The life science business of Merck operates as MilliporeSigma in the U.S. and Canada.

Material Matters™
VOL. 14 • NO. 4

# Introduction

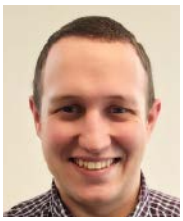

Richard Sullivan, Ph.D.
Product Manager - Materials Synthesis

Welcome to the fourth issue of *Material Matters*™ for 2019. Magnetic nanomaterials have attracted significant interest due to their many unique properties, in particular, paramagnetism. The quality and applicability of magnetic nanomaterials is directly influenced by the chosen synthesis method and pathway for chemical functionalization. Progress in this area continues to be made in fit-for-purpose magnetic nanomaterial syntheses through refinement of the control of shape, size, and functionality.

In the first article, **Professor Randal Lee** (University of Houston, USA) discusses design considerations for iron oxide magnetic nanospheres and nanocubes used for biosensing, including synthetic procedures, size, and shape. The effects of these variables are discussed for various volumetric-based and surface-based detection schemes.

**Professor Yadong Yin** (University of California Riverside, USA) examines both direct (thermal decomposition, solvothermal, hydrothermal) and indirect (templated) synthesis methods of magnetite nanocrystals. This article reviews in detail the landscape of these various synthetic methods for magnetite nanocrystal and their applications in magnetic assembly, magnetic hyperthermia, and Li-Ion batteries

Magnetic-plasmonic nanoparticles offer the combined benefits of both a magnetic probe as well as additional imaging modes usually associated with noble metal nanoparticles. **Professor Shinya Maenosono** (Japan Advanced Institute of Science and Technology) explores the synthesis, characterization, and proof-of-concept application of Ag/FeCo/Ag core/shell/shell magnetic-plasmonic nanobeads for imaging and isolation of cellular organelles (autophagosomes of COS-1 cells).

Each article in this publication is accompanied by a list of relevant Sigma-Aldrich materials available from MilliporeSigma/Merck. For additional product information, visit us at **SigmaAldrich.com/matsci**. Please bother us with your new product suggestions, as well as thoughts and comments for *Material Matters*™ at **SigmaAldrich.com/technicalservice**.

## About the Cover

Recent efforts in engineered magnetic nanostructures have emphasized high-sensitivity hybrid organic/inorganic systems for biosensing, bioimaging, drug delivery, as well as selective magnetic isolation and hyperthermia. On the cover of this issue, functionalized magnetic nanoparticles specifically bind to a differentiated target enabling magnetic isolation and sensing.

Merck KGaA
Frankfurter Strasse 250
64293 Darmstadt, Germany
Phone +49 6151 72 0

**To Place Orders / Customer Service**
Contact your local office or visit
**SigmaAldrich.com/order**

**Technical Service**
Contact your local office or visit
**SigmaAldrich.com/techinfo**

**General Correspondence**
Materials Science
**materialsscience@sial.com**

**Subscriptions**
Request your FREE subscription to *Material Matters*™ at **SigmaAldrich.com/mm**

The entire *Material Matters*™ archive is available at **SigmaAldrich.com/mm**

*Material Matters*™(ISSN 1933-9631) is a publication of Merck KGaA.

# Table of Contents

## Articles



## Featured Products



# Your Material Matters

Bryce P. Nelson, Ph.D.
Materials Science Initiative Lead

*We welcome fresh product ideas. Do you have a material or compound you wish to see featured in our Materials Science line? If it is needed to accelerate your research, it matters. Send your suggestion to* ***matsci@sial.com*** *for consideration.*

Dr. Shinae Kizaka-Kondoh & Dr. Takahiro Kuchimaru (Tokyo Institute of Technology) recommended the addition of luciferin analogues for highly-sensitive near-infrared (NIR) bioluminescence imaging (BLI) to our catalog. In comparison to D-luciferin, these analogues have good chemical stability, high water solubility, and robust emission of NIR-bioluminescence ($\lambda_{max}$ = 677 nm) with native firefly luciferase (Fluc). The first luciferin analogue substrate suggested by Dr. Kondoh, TokeOni (**808350**), successfully achieves highly-sensitive imaging of deep tissues.[1] However, the limited solubility of TokeOni (≤ 0.2 mg/mL in neutral-buffered aqueous media) constrains its applications in some biological experiments. To address this limitation, Dr. Kondoh's group has developed a second luciferin analogue substrate, seMpai (**900952**). Similar to TokeOni, seMpai emits NIR-bioluminescence ($\lambda_{max}$ ~670–680 nm) through the reaction with Fluc, but has higher solubility (≤ 20 mg/mL) in neutral-buffered aqueous media. Both reagents are chemically stable for several months when stored at -80°C. Detection of lung metastasis in mice demonstrated that the detection sensitivity of seMpai is higher than that of D-luciferin and comparable with that of TokeOni,[2] making seMpai (**900952**) a promising substrate for NIR-bioluminescence in many biological applications.

### References

(1) Kuchimaru, T. et al. *Nat. Commun.* **2016**, *7*, 11856.
(2) Saito, R. et al. *Bull. Chem. Soc. Jpn* **2019**, *92*, 608–618.

**TokeOni**

$C_{16}H_{19}ClN_2O_2S \cdot xHCl$ FW 338.85 (FB)

powder
store at −20°C

| | |
|---|---|
| 5 mg | **808350-5MG** |
| 25 mg | **808350-25MG** |
| 100 mg | **808350-100MG** |

**seMpai**

$C_{15}H_{17}N_3O_2S$ FW 303.38

powder
store at −20°C

| | |
|---|---|
| 5 mg | **900952-5MG** |
| 25 mg | **900952-25MG** |

MERCK

# THE FUTURE OF BIOIMAGING

## Nanomaterial Bioconjugation Techniques

A guide for surface modification allowing bioconjugation of inorganic nanomaterials having applications in theranostics. Discover the latest advances and protocols in nanoparticle conjugation for:

- Magnetic Imaging
- Fluorescence Imaging
- Optical-based Imaging

Order your complimentary copy from:
**SigmaAldrich.com/nanomaterials-conjugation**

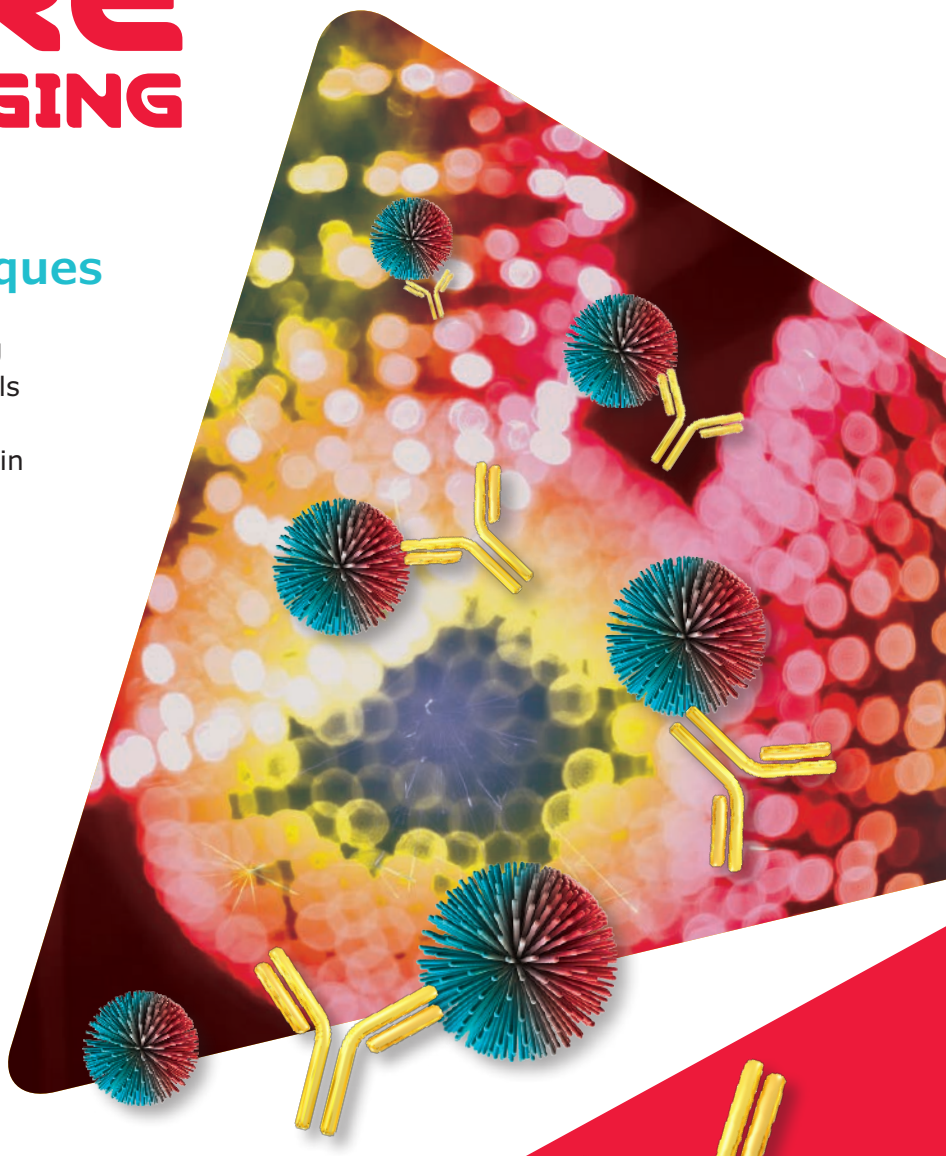



Sigma-Aldrich®
Lab & Production Materials

# Synthesis of Magnetic Nanoparticles for Biosensing

Riddhiman Medhi, Pannaree Srinoi, Tingting Liu, Hung-Vu Tran, Maria D. Marquez, and T. Randall Lee*

Department of Chemistry and the Texas Center for Superconductivity, University of Houston, 4800 Calhoun Road, Houston, Texas 77204-5003, United States
*Email: trlee@uh.edu

## Introduction

Magnetic nanoparticles (MNPs) are widely used in biomedical applications such as biosensing, bioimaging, hyperthermia, and drug delivery.[1] MNPs exhibit properties that are noticeably different from their bulk materials due to the particle size closely approaching the domain size as well as an increased surface-to-volume ratio afforded by the smaller dimensions.[2] Given that biosensors are devices that provide both qualitative and quantitative information regarding the composition of the molecules in which the sensor is situated,[3] biosensing applications require specific properties that strongly depend on size, shape, functionality, stability, and magnetization of the MNPs, as summarized in **Figure 1**.

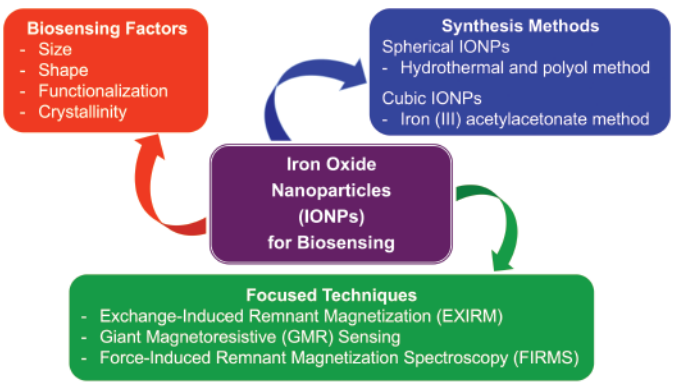


**Figure 1.** Magnetic nanoparticles for biosensing: techniques, factors affecting magnetization, and MNP synthetic methods.

Typically, MNPs are classified as diamagnetic, paramagnetic, ferromagnetic, ferrimagnetic, antiferromagnetic, and superparamagnetic based on intrinsic magnetic dipoles and the net magnetization in the presence and absence of an external magnetic field.[2] In the presence of an external magnetic field, the maximum magnetization observed when the magnetic moment of the MNPs is aligned along the direction of the external magnetic field is defined as saturation magnetization ($M_s$).[4] Upon removal of an external magnetic field, the magnetic moment of MNPs retains the previous direction and magnetization, which is defined as remnant magnetization (Mr). In general, MNPs with high $M_s$ values are preferred for biosensing applications due to their high sensitivity, which provides enhanced sensing efficiency;[5] furthermore, $M_s$ values generally increase with the size of the MNPs. Even though there is no clear consensus with regard to shape, some reports have concluded that the greater biosensing capacity of cubic vs spherical MNPs arises from the greater crystallinity of the former.[2]

Several factors must be considered in the design of MNPs for specific biosensing applications. These include determining a suitable size and shape, modifying the MNPs with biocompatible ligands, optimizing the magnetic properties, and identifying suitable magnetic detection techniques to evaluate the effectiveness of the MNPs. Iron oxide nanoparticles (IONPs) are one of the most common metal oxide MNPs used in biosensing, due to their biocompatibility, low toxicity, strong superparamagnetism, good catalytic activity, and simple

preparation processes.[1,4] However, commercially available MNPs, particularly IONPs, are magnetically weak, which limits their sensitivity for magnetic detection. Consequently, the design and synthesis of IONPs with well controlled size and shape have been pursued in order to optimize their inherent magnetic and electrical properties in efforts to generate sensors with high sensitivity. The most common techniques used to synthesize IONPs are wet chemical methods that include co-precipitation, thermal decomposition, and hydrothermal methods.[4] Various researchers are continuing to explore new methods for the synthesis of IONPs with controllable size and shape to study the effect of morphology on the magnetic properties in biosensing applications. In this article, we evaluate the synthetic procedures used to obtain homogeneous $Fe_3O_4$ nanospheres and nanocubes. We also discuss the effect of shape, size, and incorporation of a second metal (i.e., $Fe_3O_4$-based bimetallic MNPs) on the selectivity and sensitivity of IONP-based biosensors.

## Iron Oxide Nanospheres

Various $Fe_3O_4$ nanostructures, such as nanospheres,[6] nanocubes,[6] nanorods,[7] nanowires,[8] and nanoplates[9] have been reported and utilized in a wide variety of applications. For non-spherical $Fe_3O_4$ nanostructures, the shape is mainly controlled by the incorporation of surfactants, such as sodium oleate (**Cat. No. O7501**) and methyltrioctylammonium bromide (**Cat. No. 365718**).[9] For $Fe_3O_4$ nanospheres greater than 100 nm in diameter, the particles grow from a collection of nanocrystals that agglomerate into the final particle size.[10] The hydrothermal-polyol method has proven to be highly effective for obtaining large IONPs (i.e., with diameters > 100 nm). Ethylene glycol (EG) (**Cat. No. 324558**) and diethylene glycol (DEG) (**Cat. No. 32160**) are two common polyols used to synthesize large, homogenous IONPs.[6,11]

Recently, Kolhatkar et al. reported the synthesis of a series of spherical IONPs ranging in diameter from 100 nm to 300 nm obtained by the hydrothermal-polyol method, using EG as the polyol and iron chloride hexahydrate (**Cat No. 31232**) as the source of iron.[6] The authors varied reaction time, temperature, and stirring speed to prepare these IONPs. Similarly, Chen et al. reported a series of IONPs with an even wider size distribution — 120 nm, 440 nm, and 700 nm, shown in **Figure 2**.[11] The authors indicated that for IONPs smaller than 200 nm, the reducing agent and solvent, in this case EG and DEG, were critical to the preparation of 120 nm IONPs. The authors also noted a higher number of agglomeration centers in the presence of DEG when the targeted size of the IONPs was larger than 200 nm; furthermore, EG provided a stronger reducing capability and better capacity for size control. Ultimately, the size of the IONPs can be affected by many factors, such as reaction temperature, pressure, time, concentration, stirring speed, reducing agent, and solvent.[6,11]

To prepare smaller (< 30 nm) spherical IONPs, co-precipitation, thermal decomposition, and hydrothermal methods are commonly used.[10] Similar to the larger IONPs, the size of the particle can be controlled by adjusting the iron source, reaction temperature, as well as the pH of the solution.[10] The co-precipitation method is considered to be one of the most effective methods to obtain IONPs smaller than 30 nm. Nevertheless, IONPs (< 30 nm) with excellent crystallite morphology can also be obtained by the thermal decomposition method as well as the hydrothermal method.[10] Specifically, the thermal decomposition method requires an organic solvent with a high boiling point and a stabilizing agent, while the hydrothermal method requires the reaction to occur under high pressure (> 2000 psi) and high temperature (> 200 °C).[10]

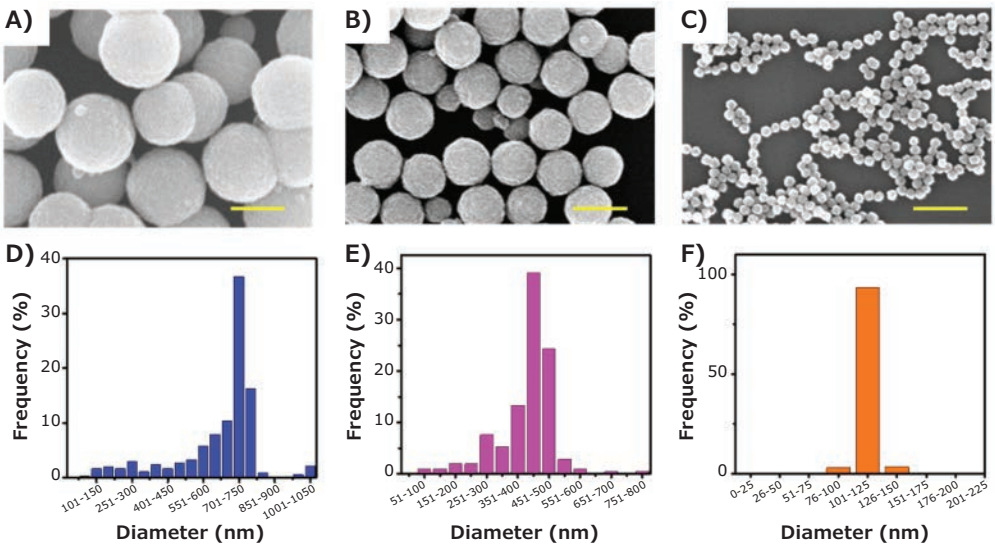


**Figure 2.** SEM images and size distributions of IONPs with diameters of 700, 440, and 120 nm, respectively. Scale bar: 500 nm. Adapted with permission from reference 11, copyright 2018 American Chemical Society.

## Iron Oxide Nanocubes

There are two preferred routes for the synthesis of uniform iron oxide nanocubes (IONCs). One approach utilizes iron (III) acetylacetonate (**Cat. No. 517003**) together with oleic acid (**Cat. No. O1008**) and benzyl ether (**Cat. No. W237108**). This approach was first used by Yang et al. in 2007,[12] where mono-crystalline, magnetite-phase $Fe_3O_4$ nanocubes (with edge length of 15 nm) were synthesized using a mixture of $Fe(acac)_3$, 1,2-hexadecanediol (**Cat. No. 213748**), oleic acid, oleyl amine (**Cat. No. O7805**), and benzyl ether; the IONPs obtained from this method are shown in **Figure 3A**. Briefly, the above mixture was heated at 110 °C for 1 h under flowing Ar. The temperature was then raised to 200 °C and maintained at that temperature for 30 min. The reaction was further heated to a reflux temperature of ~290 °C at a heating rate 15 °C/min and refluxed for 1 h. The nanocubes were precipitated by adding ethanol (**Cat. No. 459836**) and redispersed in a mixture of toluene (**Cat. No. 244511**) and hexane (**Cat. No. 296090**). This method offers at least two distinct advantages. First, it is a one-pot method, which is easier to execute than a seed-mediated growth method. Second, the size of the nanocubes can be adjusted simply by varying the heating parameters. For example, smaller nanocubes (e.g., 6.5 nm edge length) were obtained when the reflux temperature was quickly raised at a rate of 35 °C/min and a short reflux time of 20 min, due to the relatively faster rate of nucleation. Larger nanocubes (e.g., 30 nm edge length) were obtained via a slow rate of nucleation achieved by employing a 5 °C/min heating rate and a longer reflux time of 3 h.

Kim et al. used a simplified version of this procedure to obtain even larger nanocubes with edge lengths of 79 nm, 110 nm, and 160 nm, as illustrated in **Figures 3B** and **3C**.[13] For the 79 nm cubes, a degassed mixture of $Fe(acac)_3$, oleic acid, and benzyl ether was heated to 290 °C at 20 °C/min and then maintained at this temperature for 30 min. Toluene and hexane were added to this solution after cooling to precipitate the particles. Truncated cubes, with an edge length of 110 nm, were obtained by reducing the amount of benzyl ether; separately, by increasing the reaction time from 1.5 h to 2 h, cubes with an edge length of 160 nm were obtained.

Nanocubes are formed via fast growth along the [111] directions, and the projected surfaces of the nanocubes are (100) planes. Moreover, the versatile nature of this method for producing nanocubes of varying sizes—both small and large—was further illustrated by a slight modification of the recipe by adding 4-biphenylcarboxylic acid (**Cat. No. B34729**) along with a slightly greater amount of oleic acid to produce nanocubes with an edge length of 22 nm.[13] Given its versatility, many researchers have made minor modifications to this method to obtain various IONCs.[6,14] Kolhatkar et al. simplified this method

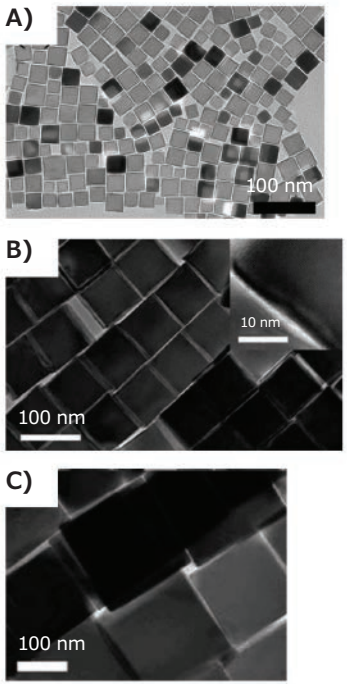


**Figure 3.** TEM images of IONCs synthesized using the ether-based reflux method by **A)** Yang et al. Adapted with permission from reference 12, copyright 2008 AIP Publishing. **B,C)** Kim et al. Adapted with permission from reference 13, copyright 2008 American Chemical Society.

further by using $Fe(acac)_3$ and oleic acid heated in benzyl ether to 290 °C.[6] By varying the reactant concentration and reaction time, these researchers were able to obtain even larger $Fe_3O_4$ nanocubes with body diagonals of 135, 150, 175, and 225 nm (edge lengths 80, 85, 100, and 130 nm, respectively), as shown in **Figure 4**. In a separate study, a reduced temperature profile in a magnesium acetate-assisted modification of this method also led to the successful synthesis of nanocubes. By adjusting the sodium oleate concentration, nanocubes with edge lengths of 22 nm, 36 nm, and 57 nm were obtained with a size deviation of less than 10%.[15]

Alternatively, IONCs with edge lengths of ~70 nm have also been synthesized using ferrocene as the iron source.[16] In this method, ferrocene (**Cat. No. F408**) and polyvinylpyrrolidone (**Cat. No. 81420**) were dissolved in water and alcohol followed by the slow addition of hydrogen peroxide. The mixture was then transferred to a Teflon-lined stainless-steel autoclave and placed in an oven at 230 °C for 24 h, and then ambiently cooled to room temperature. Notably, this method produces some polyhedron-shaped particles in addition to the cubes. Nevertheless, the ether-based reflux method remains as the preferred method for the synthesis of $Fe_3O_4$ nanocubes across multiple research groups due to its ease and reliability for producing cubic nanoparticles.[6,14,15]

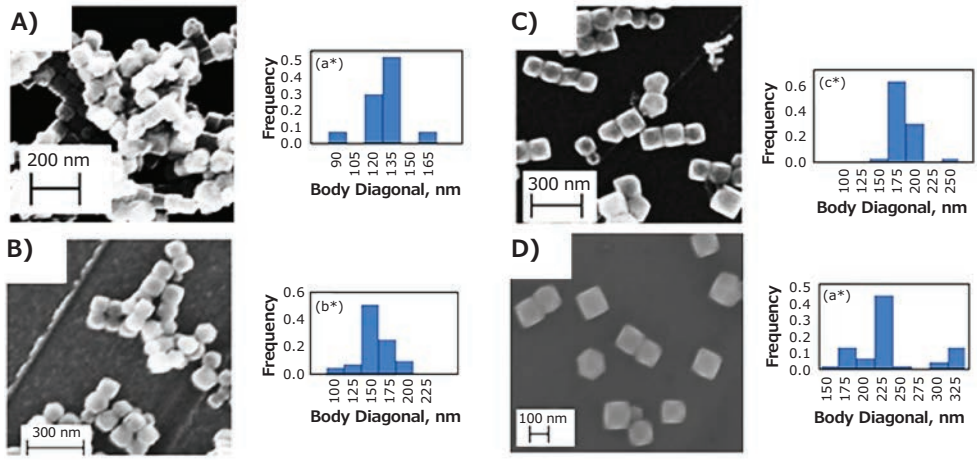


**Figure 4.** SEM images and respective size distribution plots for IONCs synthesized by Kolhatkar et al. Adapted with permission from reference 6, copyright 2017 American Chemical Society.

## Applications in Magnetic Biosensing

MNPs as biosensing tools rely on a variety of magnetic detection techniques, which can be classified into two classes: volumetric-based techniques and surface-based techniques. Volumetric-based sensors, such as the planar Hall effect (PHE) and nuclear magnetic resonance (NMR) systems, provide simple and rapid sample preparation and detection. On the other hand, surface-based sensors, such as giant magnetoresistance (GMR) and tunnel magnetoresistance (TMR) sensors, offer extremely low detection limits but require laborious sample preparation. Furthermore, superconducting quantum interference devices (SQUIDs) and atomic magnetometers (AMs) are highly sensitive instruments that can be operated using either technique, depending on the targeted application.[4] These biosensing methods rely on the magnetic properties of the material, which can be tuned by varying factors such as the size, shape, and composition of the particles.[2] In the following sections, we focus our discussion on the effects of size, shape, and composition on the magnetic properties of MNPs and ultimately on the sensing ability of these nanomaterials.

The relationship between particle size and the performance of MNPs in biosensors was recently investigated by Chen et al.[11] Specifically, Chen et al. synthesized magnetic iron oxide particles with diameters of 120, 440, and 700 nm, and then functionalized their surfaces with streptavidin for use in the specific and sensitive detection of proteins. Biofunctionalization of the MNPs was achieved via a silica-coating (from tetraethylorthosilicate, **Cat. No. 333859**), followed by the growth of a carboxy-terminated polymer generated from 3-(trimethoxysilyl)propyl methacrylate (**Cat. No. 440159**) followed by carbodiimide (**Cat. No. 03449**) coupling to the pendant amino groups on streptavidin.

The magnetic signals and responses improved significantly as the particle size was increased and were greater than those of commercially available Dynabeads. As a proof of concept, these functionalized-magnetic particles were tested in the specific detection of a targeted protein (IgG2a) in solution by displacing a magnetically labeled protein (IgG1) on the receptor, where the driving force of the exchange arose from the difference in the binding affinity of the protein to the surface-immobilized receptor (i.e., the binding affinity of IgG2a was greater than that of IgG1). These highly sensitive and specific label-free protein detection experiments were performed by using the exchange-induced remnant magnetization (EXIRM) method, which is derived from force-induced remnant magnetization spectroscopy (FIRMS).[17] The synthesized MNPs showed sensitivity improvements of 9-, 4-, and 2-fold for the 700, 400, and 100 nm magnetic particles, respectively, when compared to commercially available Dynabeads.

Kolhatkar et al. also investigated the relationship between the morphology of IONPs and their magnetic sensing ability.[6] Specifically, $Fe_3O_4$ nanocubes and nanospheres of tunable size were synthesized to obtain particles with either equivalent volumes or dimensions (i.e., body diagonal/diameter). The magnetic properties of these MNPs were compared by using vibrating sample magnetometry (VSM), which revealed a $M_s$ and coercivity for the nanocubes 1.4–3 and 1.1–8.4 times higher than those of the nanospheres, on a same-volume and same-body diagonal/diameter basis, respectively. Analysis by X-ray diffraction (XRD) and transmission electron microscopy (TEM) showed that the nanocubes were more crystalline than the nanospheres; the nanospheres are polycrystalline while the nanocubes grow as largely monocrystalline (**Figure 5A**). Consequently, the higher crystallinity of the nanocubes is

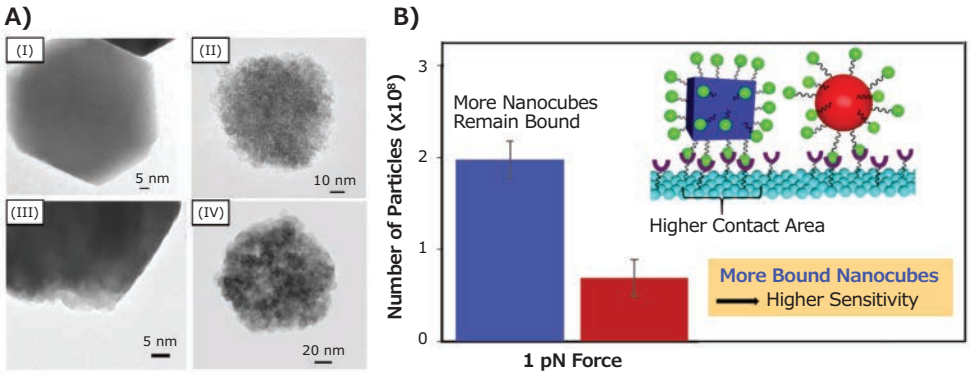


**Figure 5.** Magnetic sensing ability of $Fe_3O_4$ nanocubes and nanospheres. **A)** TEM images of (I) 150 nm cubic $Fe_3O_4$ MNPs, (II) 100 nm spherical $Fe_3O_4$ MNPs, (III) 135 nm cubic $Fe_3O_4$ MNPs, and (IV) 135 nm spherical $Fe_3O_4$ MNPs. **B)** Number of particles on the sensor at 1 pN and contact area for cubic MNPs (blue) compared to spherical MNPs (red). Adapted with permission from reference 6, Copyright 2017 American Chemical Society.

responsible for the higher $M_s$ and higher Curie temperature when compared to the corresponding nanospheres. Furthermore, the sensing potential of the synthesized MNPs were evaluated via GMR sensing and FIRMS. Both techniques revealed a distinct sensitivity advantage for the nanocubes when compared to the nanospheres. This result was attributed to the higher magnetization and binding affinity of the nanocubes (**Figure 5B**).

In addition to single-component MNPs, magnetic bimetallic nanoparticles have also been used as biosensing materials.[18] These nanoparticles typically exhibit higher magnetic moments than their single-component counterparts. Consequently, bimetallic nanoparticles usually offer improved sensitivities than the single-component MNPs. However, similarly to single-component IONPs, modification of the particle composition and structure influences the magnetic response. For example, Kolhatkar et al. synthesized and studied cubic silica-coated FeCo MNPs and found that as the size of the particles was systematically increased, the magnetic signal and response correspondingly increased.[19]

## Conclusions

To produce MNP-based biosensors with high sensitivity, the key factor is the availability of MNPs with strong magnetic responses. As demonstrated herein, sensor responses can be enhanced simply by adjusting the size and morphology of the MNPs, where larger particles outperform smaller particles, and particles with high crystallinity (e.g., nanocubes) outperform those with low crystallinity (e.g., nanospheres). Various synthetic methods have been developed to obtain both large (> 100 nm) and small (< 30 nm) MNPs having either spherical or cubic shape with narrow size distributions and large crystallite sizes. Moreover, the further development of new MNPs can lead to novel approaches to MNP-based sensing, such as the recently demonstrated "loss-of-signal" approach where IONPs are converted, in situ, to a non-magnetic product.[20]

## Acknowledgments

This research was generously supported by the Robert A. Welch Foundation (Grant No. E-1320), the Air Force Office of Scientific Research (AFOSR FA9550-18-1-0094), and the Texas Center for Superconductivity at the University of Houston.

## References

(1) Li, X.; Wei, J.; Aifantis, K. E.; Fan, Y.; Feng, Q.; Cui, F.-Z.; Watari, F. *J. Biomed. Mater. Res. A* **2016**, *104*, 1285–1296.
(2) Kolhatkar, A. G.; Jamison, A. C.; Litvinov, D.; Willson, R. C.; Lee, T. R. *Int. J. Mol. Sci.* **2013**, *14*, 15977–16009.
(3) Rick, J.; Tsai, M.-C.; Hwang, B. J. *Nanomaterials* **2016**, *6*, 5.
(4) Chen, Y.-T.; Kolhatkar, A. G.; Zenasni, O.; Xu, S.; Lee, T. R. *Sensors* **2017**, *17*, 2300.
(5) Colombo, M.; Carregal-Romero, S.; Casula, M. F.; Gutiérrez, L.; Morales, M. P.; Böhm, I. B.; Heverhagen, J. T.; Prosperi, D.; Parak, W. J. *Chem. Soc. Rev.* **2012**, *41*, 4306–4334.
(6) Kolhatkar, A. G.; Chen, Y.-T.; Chinwangso, P.; Nekrashevich, I.; Dannangoda, G. C.; Singh, A.; Jamison, A. C.; Zenasni, O.; Rusakova, I. A.; Martirosyan, K. S.; Litvinov, D.; Xu, S.; Willson, R. C.; Lee, T. R. *ACS Omega* **2017**, *2*, 8010–8019.
(7) Orza, A.; Wu, H.; Xu, Y.; Lu, Q.; Mao, H. *ACS Appl. Mater. Interfaces* **2017**, *9*, 20719–20727.
(8) Bennett, R. A.; Etman, H. A.; Hicks, H.; Richards, L.; Wu, C.; Castell, M. R.; Dhesi, S. S.; Maccherozzi, F. *Nano Letters* **2018**, *18*, 2365–2372.
(9) Palchoudhury, S.; Xu, Y.; Rushdi, A.; Holler, R. A.; Bao, Y. Chem. Commun. 2012, 48, 10499–10501.
(10) Liu, J.; Qiao, S. Z.; Hu, Q. H.; Lu, G. Q. *Small* **2011**, *7*, 425–443.
(11) Chen, Y.-T.; Medhi, R.; Nekrashevich, I.; Litvinov, D.; Xu, S.; Lee, T. R. *Anal. Chem.* **2018**, *90*, 6749–6756.
(12) Yang, H.; Ogawa, T.; Hasegawa, D.; Takahashi, M. *J. Appl. Phys.* **2008**, *103*, 07D526.
(13) Kim, D.; Lee, N.; Park, M.; Kim, B. H.; An, K.; Hyeon, T. *J. Am. Chem. Soc.* **2009**, *131*, 454–455.
(14) Ho, C.-H.; Tsai, C.-P.; Chung, C.-C.; Tsai, C.-Y.; Chen, F.-R.; Lin, H.-J.; Lai, C.-H. *Chem. Mater.* **2011**, *23*, 1753–1760.
(15) Lee, K.; Lee, S.; Oh, M. C.; Ahn, B. *Metals* **2018**, *8*, 107.
(16) Xiong, Y.; Ye, J.; Gu, X.; Chen, Q.-W. *J. Phys. Chem. C* **2007**, *111*, 6998–7003.
(17) Chen, Y.-T.; Jamison, A. C.; Lee, T. R.; Xu, S. *ACS Cent. Sci.* **2016**, *2*, 75–79.
(18) Srinoi, P.; Chen, Y.-T.; Vittur, V.; Marquez, M. D.; Lee, T. R. *Appl. Sci.* **2018**, *8*, 1106
(19) Kolhatkar, A. G.; Nekrashevich, I.; Litvinov, D.; Willson, R. C.; Lee, T. R. *Chem. Mater.* **2013**, *25*, 1092–1097.
(20) Kolhatkar, A. G.; Jamison, A. C.; Nekrashevich, I.; Kourentzi, K.; Litvinov, D.; Brazdeikis, A.; Willson, R. C.; Lee, T. R. *Analyst* **2016**, *141*, 5246–5251.

## Iron Precursors for MNPs

| Name | Composition | Form | Purity | Cat. No. |
|---|---|---|---|---|
| Iron(II) acetate | $Fe(CO_2CH_3)_2$ | solid | ≥99.99% trace metals basis | **517933-5G**<br>**517933-25G** |
| | $Fe(CO_2CH_3)_2$ | solid | 95% | **339199-10G**<br>**339199-50G** |
| Iron(III) acetylacetonate | $Fe(C_5H_7O_2)_3$ | powder | ≥99.9% trace metals basis | **517003-10G**<br>**517003-50G** |
| | $Fe(C_5H_7O_2)_3$ | powder | 97% | **F300-25G**<br>**F300-100G**<br>**F300-500G** |
| Iron(III) chloride | $FeCl_3$ | powder or crystals | ≥99.9% trace metals basis | **701122-1G**<br>**701122-5G**<br>**701122-25G** |
| Iron(III) chloride hexahydrate | $FeCl_3 \cdot 6H_2O$ | powder or crystals | ≥99% | **31232-250G**<br>**31232-1KG**<br>**31232-6X1KG**<br>**31232-25KG** |
| Iron(III) nitrate nonahydrate | $Fe(NO_3)_3 \cdot 9H_2O$ | solid | ≥99.999% trace metals basis | **529303-25G** |

## Surfactants for MNPs

| Name | Composition | Purity | Cat. No. |
|---|---|---|---|
| Oleic acid | $CH_3(CH_2)_7CH=CH(CH_2)_7COOH$ | ≥99%, GC | **O1008-1G**<br>**O1008-5G**<br>**O1008-25G** |
| Oleylamine | $CH_3(CH_2)_7CH=CH(CH_2)_7CH_2NH_2$ | 70% | **O7805-5G**<br>**O7805-100G**<br>**O7805-500G** |
| Sodium oleate | $CH_3(CH_2)_7CH=CH(CH_2)_7COONa$ | ≥99% | **O7501-250MG**<br>**O7501-1G**<br>**O7501-5G**<br>**O7501-10G** |
| Trioctylamine | $[CH_3(CH_2)_7]_3N$ | 98% | **T81000-25G**<br>**T81000-100G**<br>**T81000-500G**<br>**T81000-2.5KG** |

## Polyols

| Name | Composition | Purity | Cat. No. |
|---|---|---|---|
| Diethylene glycol | $(HOCH_2CH_2)_2O$ | puriss. p.a.; ≥99.0%, GC | **32160-500ML**<br>**32160-1L** |
| Ethylene glycol | $HOCH_2CH_2OH$ | 99.8% | **324558-100ML**<br>**324558-12X100ML**<br>**324558-1L**<br>**324558-6X1L**<br>**324558-2L** |
| 1,2-Hexadecanediol | $CH_3(CH_2)_{13}CHOHCH_2OH$ | 90% | **213748-50G** |
| 1,2-Tetradecanediol | $CH_3(CH_2)_{11}CH(OH)CH_2OH$ | 90% | **260290-100G** |
| Tetraethylene glycol | $HO(CH_2CH_2O)_3CH_2CH_2OH$ | 99% | **110175-100G**<br>**110175-1KG**<br>**110175-3KG**<br>**110175-20KG** |

## Poly(ethylene glycol)

### Carboxylic Acid Functionalized PEG

| Name | Structure | Molecular Weight | Cat. No. |
|---|---|---|---|
| O-(2-Carboxyethyl)-O′-methyl-undecaethylene glycol | 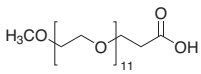 | - | **689556-250MG** |
| Methoxypolyethylene glycol 5,000 acetic acid | 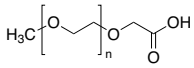 | 5,000 | **70718-1G-F**<br>**70718-5G-F**<br>**70718-25G-F** |
| Methoxypolyethylene glycol 5,000 propionic acid | 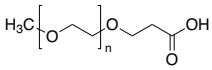 | 5,000 | **88908-1G-F**<br>**88908-5G-F** |

| Name | Structure | Molecular Weight | Cat. No. |
|---|---|---|---|
| O-Methyl-O′-succinylpolyethylene glycol 2′000 | 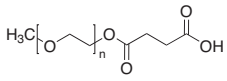 | $M_r$ ~2,100 | **17928-5G-F** |
| O-Methyl-O′-succinylpolyethylene glycol 5′000 | | $M_r$ ~5,100 | **17929-1G-F**<br>**17929-5G-F** |
| O-[2-(3-Succinylamino) ethyl]-O′-methyl-polyethylene glycol | 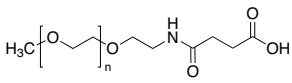 | PEG average $M_n$20,000 | **21954-1G** |

## NHS Ester Functionalized PEG

| Name | Structure | Molecular Weight | Cat. No. |
|---|---|---|---|
| Methoxypolyethylene glycol 5,000 acetic acid N-succinimidyl ester | 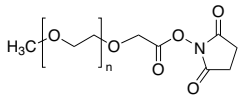 | PEG average $M_n$5,000 | **85973-1G** |
| O-[(N-Succinimidyl) succinyl-aminoethyl]-O′-methylpolyethylene glycol | 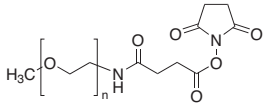 | average $M_n$ 750 | **712531-250MG** |
| O-[(N-Succinimidyl) succinyl-aminoethyl]-O′-methylpolyethylene glycol 2′000 | 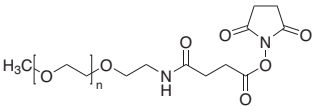 | 2,000 | **41214-1G-F** |

## Azide Functionalized PEG

| Name | Structure | Molecular Weight | Cat. No. |
|---|---|---|---|
| O-(2-Azidoethyl)-O′-methyl-triethylene glycol | 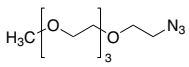 | average $M_n$ 200 | **712590-100MG** |
| O-(2-Azidoethyl)-O′-methyl-undecaethylene glycol | 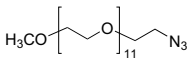 | - | **712604-100MG** |
| O-(2-Azidoethyl) nonadecaethylene glycol | 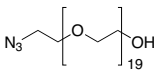 | - | **726249-250MG** |
| Methoxypolyethylene glycol azide | 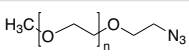 | PEG average $M_n$10,000 | **726168-250MG** |
| | 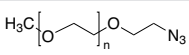 | PEG average Mn20,000 | **726176-250MG** |
| mPEG12-Azide | 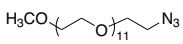 | average $M_n$ 12,000 | **JKA13019-500MG** |
| mPEG5-Azide | 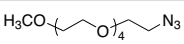 | average $M_n$ 5,000 | **JKA13016-500MG** |
| mPEG6-Azide | 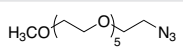 | average $M_n$ 6,000 | **JKA13017-500MG** |
| mPEG7-Azide | 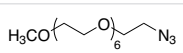 | average $M_n$ 7,000 | **JKA13018-500MG** |
| Poly(ethylene glycol) methyl ether azide | 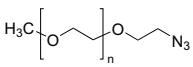 | PEG average $M_n$350 (n~8)<br>average $M_n$ 400 | **767557-1ML** |
| | 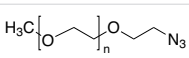 | PEG average $M_n$1,000 | **733407-1G** |

## Iron Oxide Particles Sized for Biosensing

| Name | Purity | Dimensions | Cat. No. |
|---|---|---|---|
| Iron(II,III) oxide | nanopowder<br>spherical, 97% trace metals basis | particle size 50 - 100 nm (SEM) | **637106-25G**<br>**637106-100G**<br>**637106-250G** |
| Iron(II,III) oxide | powder, 95% | <5 µm | **310069-25G**<br>**310069-500G**<br>**310069-2.5KG** |

# polymers with possibilities

## Functionalized Poly(ethylene glycol)s for Drug Delivery

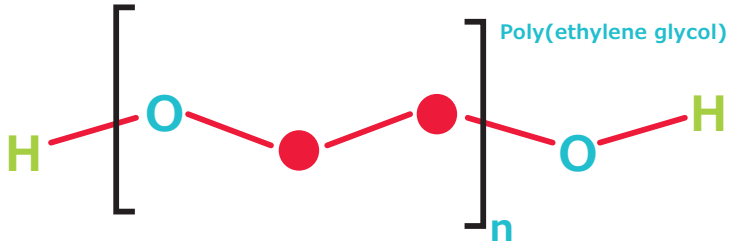


**Polymer of choice for optimal and reproducible results.**

When it comes to drug delivery technologies and solutions, poly(ethylene glycol)s or PEGs are the polymer of choice for optimal and reproducible results. With excellent pharmacokinetic properties, they are ideal materials for bioconjugation, peglylation, crosslinking, and hydrogel formation.

Let us help you transform your work into new therapeutic discoveries with our diverse PEG selection.

### Features

- Well characterized, high-purity materials with a wide variety of functional groups
- High biocompatibility, with little to no immunogenicity
- $M_n$ ranging from 1-40 kDa
- Reactivity
  - For amine, N-terminal amine, and thiol pegylation
  - For click chemistry and photochemistry
  - Heterobifunctional and multi-arm PEG crosslinkers
- Narrow polydispersity

For a complete list of available materials, visit: **SigmaAldrich.com/PEG**

# Synthesis and Application of Shape-Controlled $Fe_3O_4$ Nanostructures

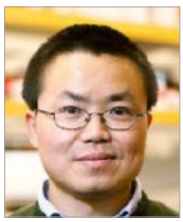

Fan Yang, Yadong Yin*

Department of Chemistry, University of California Riverside, Riverside, CA 92521, USA
*Email: yadongy@ucr.edu

## Introduction

Magnetite ($Fe_3O_4$) nanocrystals have extensive applications in drug and gene delivery,[1] field-directed assembly,[2] energy storage,[3] and catalysis[4] due to their excellent magnetic properties, ready availability, and environmentally friendly qualities. Scientists have invested significant effort into developing reliable synthetic strategies of $Fe_3O_4$ nanocrystals, with various sizes and shapes, to obtain desirable nanocrystal properties. This review provides a discussion of both the direct and indirect synthesis of magnetite nanocrystals with well-controlled shapes, including nanospheres, nanocrystal clusters, nanorods and nanodiscs, as well as their application in magnetic assembly, magnetic hyperthermia treatment, and lithium-ion batteries.

## Synthesis of Single Crystal $Fe_3O_4$ Polyhedrons

Since magnetite belongs to the hexoctahedral crystal class, single crystal magnetite nanoparticles tend to take an isometric morphology such as cube, octahedron, or tetrahedron. Among various synthetic approaches, thermal decomposition of iron precursors in high boiling-point organic solvents has been demonstrated to be an effective method for producing monodisperse $Fe_3O_4$ nanoparticles with high crystallinity. The synthetic mechanism is explained with the La Mer model, which typically includes three stages, nucleation, fast growth, and slow growth. The morphology of nanoparticles is determined in the slow growth stage, where the growth rate of crystals slows down due to the consumption of monomers. In this stage, facet-selective growth and Ostwald ripening process take place — both of which expose low surface energy facets and produce thermodynamically stable nanocrystals.

Since {100} facets are the most stable of $Fe_3O_4$ crystals, nanocubes enclosed by {100} facets are achieved by carefully controlling the growth rate in the slow growth stage. As illustrated in **Figure 1A–C**, single-crystalline $Fe_3O_4$ nanocubes can be obtained by injecting iron acetylacetonate in benzyl ether solution into hot benzyl ether (**Cat. No. W237108**) solution containing oleic acid (OA, **Cat. No. 1008**) and oleylamine (**Cat. No. O7805**) as surfactants at a steady rate.[5] **Figure 1A–C** demonstrates the morphology evolution of $Fe_3O_4$ crystals at 10 min, 30 min, and 2 h after the reaction is triggered. The increase in crystal size occurs mainly in the first 30 min, while the particles start to take cubic shape after this period. The size of nanocubes can be tuned by changing precursor concentration and injection rate, which changes the monomer concentration at the beginning of the slow growth stage.

To obtain $Fe_3O_4$ nanocrystals enclosed by other facets, the surface energy of facets must be altered. Surfactants have been long-recognized as a significant factor for changing the surface energy order of facets by selectively binding to certain facets through coordination. It has been reported that despite having the same organic compound, oleic acid and sodium oleate (NaOL, **Cat. No. O7501**) had different facet selectivity.[6] OA can universally bond to all facets of $Fe_3O_4$ crystals, leading to spherical nanoparticles. Meanwhile, sodium oleate can selectively bind to {111} facets of $Fe_3O_4$ resulting in hexagonal

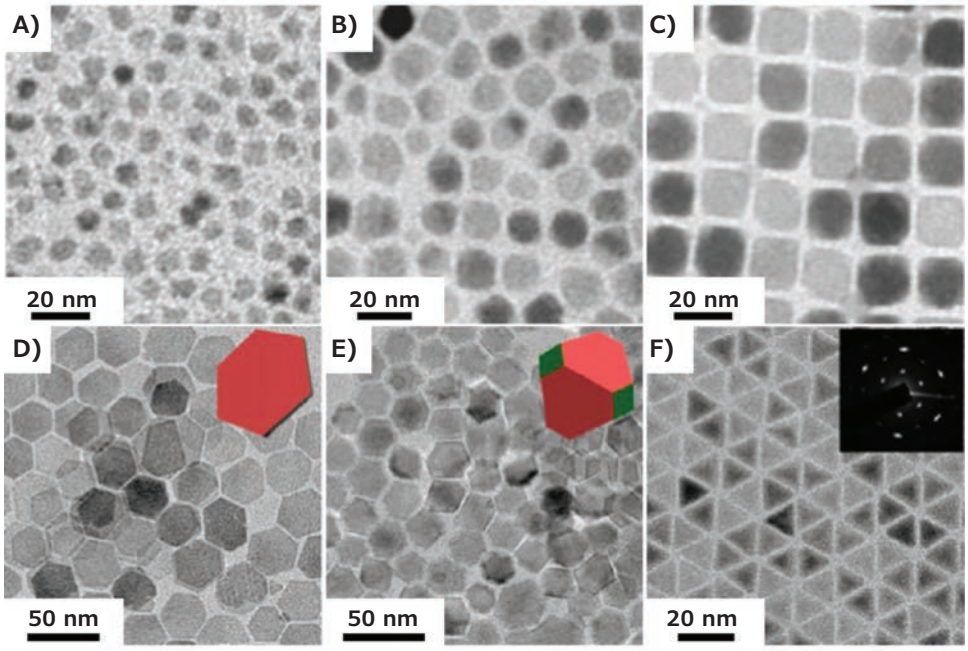


**Figure 1.** Transmission electron microcrospy (TEM) images of $Fe_3O_4$ NPs withdrawn from the reaction solution at **A**) 5 min, **B**) 30 min and **C**) 1 h after the injection was triggered. Reproduced with permission from reference 5, copyright 2011 American Chemical Society. TEM images of **D**) $Fe_3O_4$ plates, **E**) truncated octahedrons and **F**) tetrahedrons. **G**) Schematic illustration of the proposed growth model for MNCs. Reproduced with permission from reference 6, copyright 2015 American Chemical Society.

nanoplates, truncated octahedrons, or tetrahedrons depending on the sodium oleate to iron oleate (NaOL/FeOL) ratio added in the system. **Figure 1D–F** shows the morphology of $Fe_3O_4$ crystals prepared with NaOL/FeOL ratio of 1:10, 2:10, and 6:10, respectively. With increasing ratio of NaOL, the morphology of nanocrystals evolves from nanoplates to truncated octahedrons and eventually tetrahedrons, all of which are enclosed by {111} planes, evident in the high-resolution transmission electron microscopy (HRTEM) images and SAED patterns.

A comprehensive investigation into the synthetic conditions reported by Swihart, et al. provides a thorough review of the influence of solvents, diols, and surfactants in the crystal growth.[7] It was revealed that the by-product of the exposure of benzyl ether to oxygen can influence the morphology and size of $Fe_3O_4$ nanocrystals. The presence of benzaldehyde (**Cat. No. 418099**), a by-product present in oxidized benzyl ether, increases the average size and promotes faceting of the nanocrystals. Due to the difference in functional groups, oleic acid and oleylamine behave contrarily in the synthesis of $Fe_3O_4$ nanocrystals. Oleic acid, with a stronger coordination bond with the $Fe^{3+}$, increases the size of nanocrystals while oleylamine does the opposite. While other factors mainly influence the size of the final products, diol species are crucial to the morphology of prepared $Fe_3O_4$ nanocrystals. Diols with shorter carbon chains such as 1,2-tetradecanediol (**Cat. No. 260290**), promote the exposure of {100} facets, leading to cubic nanocrystals. Meanwhile, 1,2-hexadecanediol (**Cat. No. 213748**), with longer carbon chains, produce octahedral nanoparticles by slowing down the growth on {111} facets.

## Synthesis of Superparamagnetic $Fe_3O_4$ Nanoclusters

It is well known that when crystal size is reduced below a critical size (around 20 nm), $Fe_3O_4$ crystals will exhibit superparamagnetism. The fast and reversible assembly behavior also makes them a promising candidate for the fabrication of magnetically responsive smart materials. Assembling the nanoparticles into a secondary structure grants the potential of harvesting collective and size-dependent properties in addition to the superparamagnetic properties of the nanoparticles.

Yin's group reported the synthesis of poly(acrylic acid) (PAA, **Cat. No. 323667**) capped $Fe_3O_4$ colloidal nanocrystal clusters (CNCs) with tunable size by hot injection of NaOH/diethylene glycol solution (DEG, **Cat. No. 32160**) into reaction mixture containing DEG, $FeCl_3$ (**Cat. No. 451649**), and PAA.[2] The TEM image (**Figure 2A**) shows the morphology of as-prepared CNCs, and **Figure 2B** shows the proposed structure of the clusters. As shown in **Figure 2C**, regardless of the overall size at about 180 nm, the CNCs shows superparamagnetism due to the small grain size of $Fe_3O_4$ crystals. The numerous efforts to synthesize CNCs with similar superparamagnetic properties has been previously documented. For example, as reported by Zhao's

group,[8] magnetite CNCs were synthesized by a solvothermal process by reduction of $FeCl_3$ at 200 °C with ethylene glycol (**Cat. No. 324558**) in the presence of sodium acetate (NaAc, **Cat. No. 229873**) as an alkali source and trisodium citrate (**Cat. No. S4641**) as capping ligand. Carboxyl groups in sodium citrate have a high affinity towards $Fe^{3+}$ and provide strong electrostatic repulsion force by increasing the surface charge of the CNCs. The size of each $Fe_3O_4$ nanocrystal was determined to be 5–10 nm by HRTEM images (**Figure 2D**). In another solvothermal approach reported by Fang's group,[9] it was found that the amount of NaAc determined the grain size of $Fe_3O_4$ crystals, and grain size up to 30 nm was achieved (**Figure 2E**). In the meantime, the overall size of the secondary structures can be tuned by changing the amount of EDTA-2Na (**Cat. No. E4884**) or the sonication treatment time before the solvothermal process.

## Indirect Synthesis of Anisotropic $Fe_3O_4$ Nanocrystals

Despite advances in the synthesis of $Fe_3O_4$ nanocrystals, only a few works have reported the direct synthesis of anisotropic nanocrystals such as nanorods,[10] nanowires,[11] and nanoplates[12] due to difficulties in symmetry breaking of the magnetite's isometric crystal structure. However, Fe-based crystals belonging to other crystal classes can grow into anisotropic nanocrystals, as a result of the low symmetry of their crystal structure. Taking advantage of the crystal structure of various Fe based crystals such as FeOOH, $Fe_2O_3$, and Fe based metal-organic framework, uniform and monodisperse anisotropic nanocrystals can be prepared then transformed into $Fe_3O_4$ by reduction or high-temperature annealing.

Yin's group reported a universal surface protected reduction strategy where PAA was used as capping ligand during the high temperature of β-FeOOH nanorods in DEG.[13] Typically, reduction

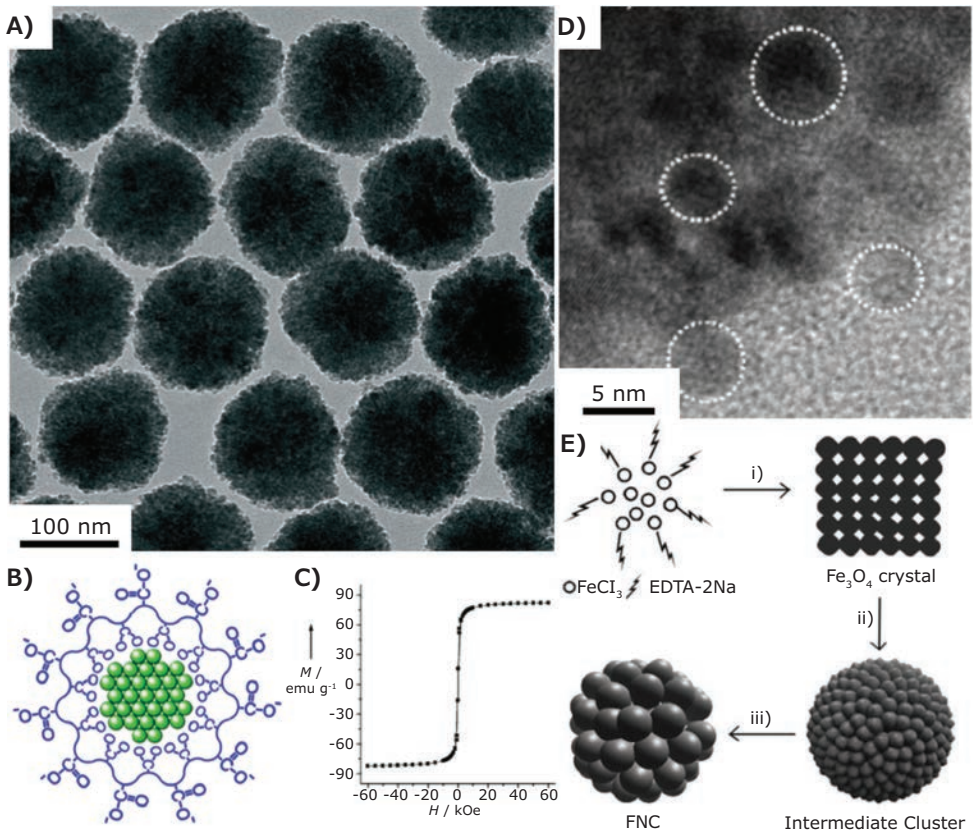


**Figure 2.** **A**) TEM image and **B**) schematic illustration of poly(acrylate) capped $Fe_3O_4$ colloidal nanocrystal clusters. **C**) Hysteresis loop of 180-nm CNCs measured at room temperature exhibiting superparamagnetic behavior. Reproduced with permission from reference 2, copyright 2007 John Wiley & Sons, Inc. **D**) HRTEM image of 250 nm $Fe_3O_4$. Reproduced with permission from reference 8, copyright 2009 John Wiley & Sons, Inc. **E**) Schematic illustration of the formation and structure evolution of CNCs. **i**) EDTA-2Na stabilized $Fe_3O_4$ crystals are formed through the hydrolysis of $FeCl_3$ under solvothermal condition. **ii**) Aggregation of $Fe_3O_4$ crystals to form loosely packed intermediate clusters. **iii**) Intermediate clusters go through a reorganization process to form CNCs. Reproduced with permission from reference 9, copyright 2013 American Chemical Society.

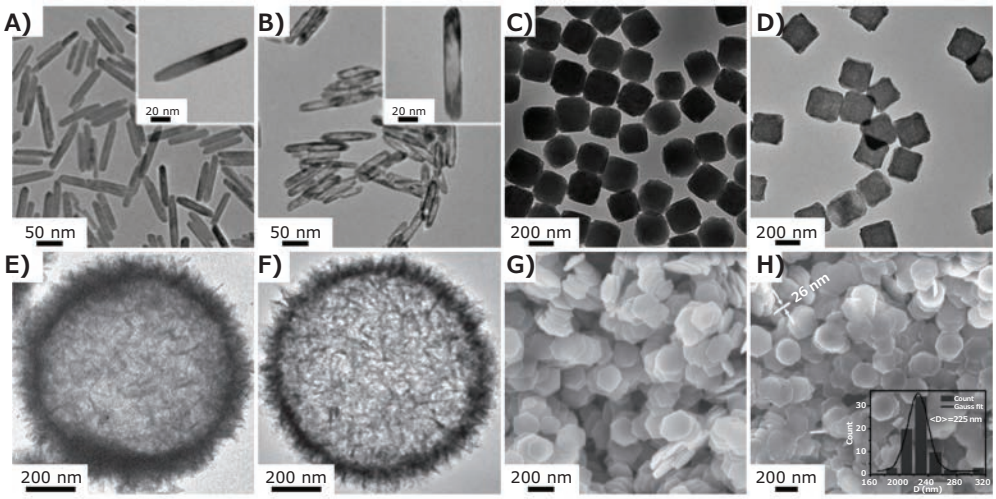


**Figure 3.** A–D) TEM images of β-FeOOH nanorods and PB nanocubes before (**A**, **C**) and after (**B**, **D**) surface-protected conversion. Reproduced with permission from reference 13, copyright 2017 American Chemical Society. TEM images of **E**) Fe-glycerate hollow spheres and **F**) $Fe_3O_4$ hollow spheres. Reproduced with permission from reference 3, copyright 2015 John Wiley & Sons, Inc. SEM images of iron oxide nanodiscs **G**) before and **H**) after reduction. The inset in (**H**) is the diameter distribution of the nanodiscs after reduction. Reproduced with permission from reference 14, copyright 2014 John Wiley & Sons, Inc.

of β-FeOOH in DEG requires a protective layer such as silica to prevent β-FeOOH from being dissolved due to the formation of Fe-glycolate. In this work, the rod morphology of β-FeOOH can be well maintained by simply introducing PAA into the reaction. Due to the strong bonding between $Fe^{3+}$ and carboxyl groups of PAA, the outmost layer of β-FeOOH nanorods was protected by PAA, preventing the formation of Fe-glycolates. As shown in **Figure 3A–B**, the reduction of β-FeOOH nanorods in DEG with the presence of PAA results in hollow $Fe_3O_4$ nanorods with well-preserved outer shells. The method also shows versatility towards other Fe based compounds including α-$Fe_2O_3$ nanospheres and Prussian blue nanocubes, as shown in **Figure 3C–D**.

Conversely, Ma et al. took advantage of the formation of Fe-glycerate and developed a two-step method to synthesize hollow $Fe_3O_4$ microspheres consisting of small nanoplates.[3] The first step involved the self-templated formation of Fe-glycerate in a solvothermal reaction of the mixture of $Fe(NO_3)_3$ (**Cat. No. 529303**), glycerol (**Cat. No. G7893**), isopropanol (**Cat. No. 733458**), and a small amount of water. After investigating the particles obtained at different stages, it was found that the hollow Fe-glycerate originated from amorphous metal alkoxide between iron and isopropanol (Fe-IPA) complex spheres. Under elevated temperature, Fe-glycerate grew on the surface of Fe-IPA spheres while Fe-IPA spheres gradually disappeared. After the Fe-glycerate hollow spheres were obtained, Fe-glycerate decomposed under annealing condition in $N_2$ (**Cat. No. 295574**) atmosphere at 350 °C. The hollow sphere morphology can be well preserved without server aggregation.

Although α-$Fe_2O_3$ nanocrystals with well-defined shapes and narrow size distribution are relatively easy to obtain, the transformation from α-$Fe_2O_3$ to $Fe_3O_4$ by traditional thermal annealing in reductive gas requires high temperature, which leads to the sintering of nanoparticles. The hydrogen-wet reduction method, on the other hand, could effectively avoid the sintering problem due to moderate reaction temperature (≈340 °C) and the usage of surfactants. As reported by Yang et al.,[14] monodisperse $Fe_2O_3$ nanodiscs were first synthesized through hydrothermal reaction. NaAc in this reaction serves both as alkali source and capping ligand that binds to specific facets of α-$Fe_2O_3$ crystals and facilitates the anisotropic growth of α-$Fe_2O_3$. As-prepared nanodiscs were then heated in a mixture of trioctylamine (**Cat. No. T81000**) and oleic acid fluxed under sufficient gas flow of $H_2$ (5%) and Ar (95%) at 340 °C. As shown in **Figure 3G–H**, no morphology or aggregation can be observed after reduction of the nanodiscs.

## Applications of $Fe_3O_4$ Nanocrystals

$Fe_3O_4$ nanocrystals are widely used in magnetic resonance imaging, drug/gene delivery, and data storage because of their strong magnetic properties. However, there are several applications that do not rely solely on the magnetic properties or utilize less desired properties in a traditional sense.

Photonic crystals, typically constructed by controlled drying or supersaturation of uniform colloidal particles, show highly saturated color due to their unique photonic bandgap. As reported in Yin's work, PAA capped $Fe_3O_4$ CNCs are ideal for the construction of magnetically responsive 1D photonic crystals.[2] The superparamagnetic nature of CNCs and strongly negatively charged surfaces provided by PAA allow for fast and reversible assembly of CNCs. The photonic bandgap can be tuned through the whole visible range by changing magnetic field strength applied as shown in **Figure 4A–B**.

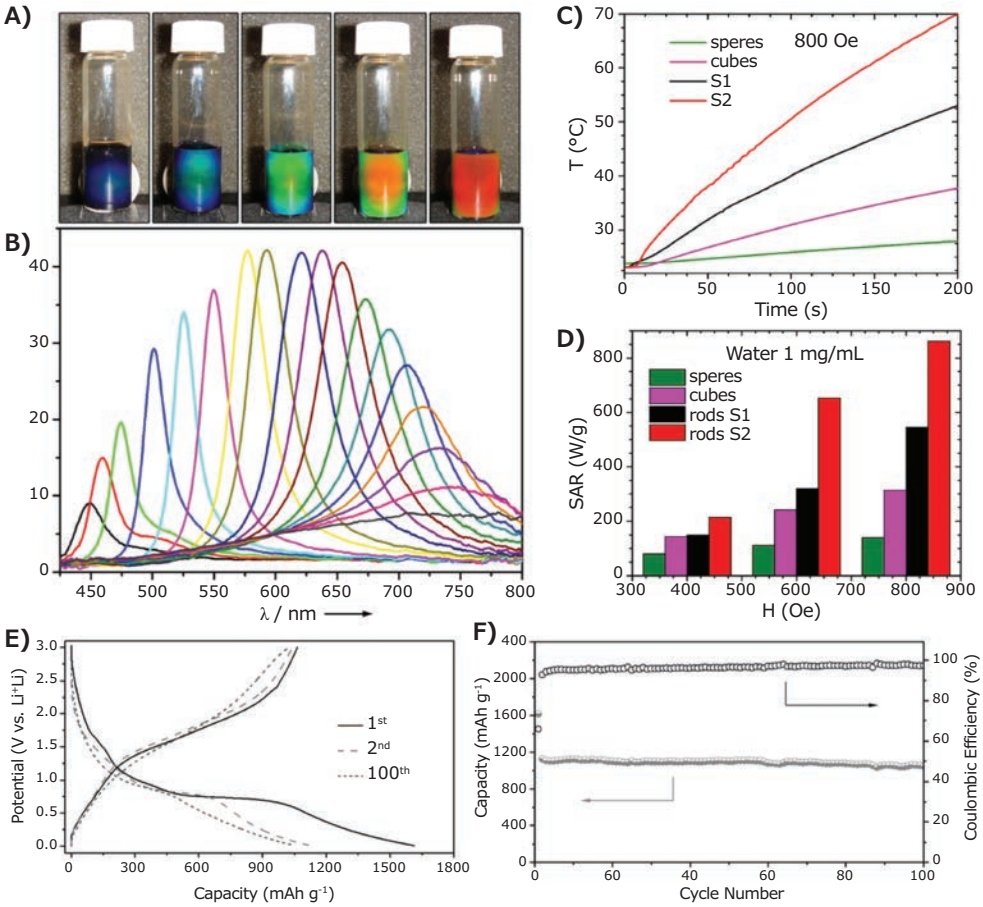


**Figure 4.** A) Photographs of colloidal crystals formed in response to an external magnetic field; the magnet-sample distance decreases gradually from right to left. **B**) Dependence of the reflection spectra at normal incidence of the colloidal crystals on the distance of the sample from the magnet. Diffraction peaks blue-shift (from right to left) as the distance decreases from 3.7 to 2.0 cm with a step size of 0.1 cm. The average diameter of the CNCs in this sample is 120 nm. Reproduced with permission from reference 2, copyright 2007 John Wiley & Sons, Inc. **C**) Heating curves for the $Fe_3O_4$ spheres, cubes, and nanorods of similar volume (1 mg/mL) in water measured at alternating currect (AC) field of 800 Oe. **D**) SAR vs. field plot for the $Fe_3O_4$ spheres, cubes, and nanorods of roughly the same volume (~2000 $nm^3$). Reproduced with permission from reference 10, copyright 2016 American Chemical Society. Electrochemical lithium storage properties of as-prepared hierarchical $Fe_3O_4$ hollow spheres: **E**) charge-discharge voltage profiles for the first, second, and 100th cycles at a constant current density of 500 $mA{\cdot}g^{-1}$; **F**) cycling performance at a current density of 500 $mA{\cdot}g^{-1}$. Reproduced with permission from reference 3, copyright 2015 John Wiley & Sons, Inc.

Magnetic hysteresis, a common phenomenon that occurs when an external magnetic field is applied on a ferrimagnet, is undesirable in many industrial applications as it partially dissipates the work into the environment as thermal energy. However, in the medical field, the application of this phenomenon shows promise in cancer treatment, due to the fact that magnetic nanoparticles can locally transform electromagnetic energy into heat in order to damage or kill cancer cells nearby.[10,14,15]

Research published by Srikanth's group[10] pointed out that the anisotropic nanoparticles like $Fe_3O_4$ nanorods exhibit superior magnetic hyperthermia to isotropic structures such as nanospheres and nanocubes. As shown in **Figure 4C**, nanorods with an aspect ratio of 11 (S2) have the highest heating rate among all four morphologies. The specific absorption rate (SAR) vs. field strength plot (**Figure 4D**) also suggests that $Fe_3O_4$ nanorods (S1 and S2) outperform spheres and cubes, especially when the magnetic field applied is strong. The paper also highlights the importance of orientation of nanorods. When the $Fe_3O_4$ nanorods are fixed in 2% agar gel (**Cat. No. A5054**), nanorods oriented along the direction of the magnetic field show higher SAR than randomly oriented nanorods.

Besides the magnetic properties, $Fe_3O_4$ as a transition metal oxide is a promising candidate for use as anode materials in high-performance lithium-ion batteries. $Fe_3O_4$ is one of the few transition metal oxides that exhibits high electronic conductivity. As reported by Lou's group,[3] hollow $Fe_3O_4$ microspheres consisting of thin nanoplates exhibit excellent electrochemical properties as potential anode materials for lithium-ion batteries as shown by their high specific capacity (**Figure 4E**), remarkable cyclability (**Figure 4F**), and superior rate capability. In addition to the advantages intrinsic to $Fe_3O_4$, the hollow structure and nanoplate subunits increase the contact surface between the active material and the electrolyte, which promote the electrochemical reactivity. Moreover, the 2D subunits ensure short transport length for $Li^+$ ions and electrons, resulting in enhanced rate capability.

## Conclusion

In summary, $Fe_3O_4$ is one of the most studied magnetic materials due to its low cost, strong magnetic properties, and well-studied crystal structures. Polyol processes that enable high-temperature decomposition of Fe compounds are beneficial for the preparation of single-crystal polyhedrons of $Fe_3O_4$. The selective exposure of certain facets can be achieved with suitable surfactants. Besides polyhedrons, a unique $Fe_3O_4$ nanocrystal cluster structure can be obtained through a high-temperature hydrolysis reaction. Interestingly, $Fe_3O_4$ CNCs can maintain superparamagnetic properties despite their overall size of over 100 nm as a result of the fine crystal size of the subunits. In addition to direct synthesis of $Fe_3O_4$ nanocrystals, an indirect synthetic strategy can bring more complexity and tunability to the nanoparticle morphologies. Anisotropic structures with well-defined morphology and narrow size distribution or complex hierarchy structures can first be obtained, and subsequently transformed into $Fe_3O_4$ through polyol reduction or hydrogen-wet reduction processes. The strong magnetic response of $Fe_3O_4$ nanocrystals makes them ideal candidates for magnetic field induced assemblies, with promising applications in smart materials. Moreover, the biocompatibility of $Fe_3O_4$ and their magnetic hysteresis behavior opens doors to medical applications such as magnetic hyperthermia treatments. In addition to the magnetic properties, $Fe_3O_4$ has also shown excellent performance as an anode material for lithium-ion batteries due to its unique electronic conductivity and high theoretical capacity as a transition metal oxide.

## Reference


(1) Ulbrich, K.; Holá, K.; Šubr, V.; Bakandritsos, A.; Tuček, J.; Zbořil, R. *Chem. Rev.* **2016**, *116*, 5338.
(2) Ge, J.; Hu, Y.; Yin, Y. *Angew. Chem. Int. Ed.* **2007**, *46*, 7428.
(3) Ma, F.-X.; Hu, H.; Wu, H. B.; Xu, C.-Y.; Xu, Z.; Zhen, L.; Lou, X. W. *Adv. Mater.* **2015**, *27*, 4097.
(4) Pham, A. L.-T.; Lee, C.; Doyle, F. M.; Sedlak, D. L. *Environ. Sci. & Technol.* **2009**, *43*, 8930.
(5) Ho, C.-H.; Tsai, C.-P.; Chung, C.-C.; Tsai, C.-Y.; Chen, F.-R.; Lin, H.-J.; Lai, C.-H. *Chem. Mater.* **2011**, *23*, 1753.
(6) Zhou, Z.; Zhu, X.; Wu, D.; Chen, Q.; Huang, D.; Sun, C.; Xin, J.; Ni, K.; Gao, J. *Chem. Mater.* **2015**, *27*, 3505.
(7) Qiao, L.; Fu, Z.; Li, J.; Ghosen, J.; Zeng, M.; Stebbins, J.; Prasad, P. N.; Swihart, M. T. *ACS Nano* **2017**, *11*, 6370.
(8) Liu, J.; Sun, Z.; Deng, Y.; Zou, Y.; Li, C.; Guo, X.; Xiong, L.; Gao, Y.; Li, F.; Zhao, D. *Angew. Chem. Int. Ed.* **2009**, *48*, 5875.
(9) Lin, M.; Huang, H.; Liu, Z.; Liu, Y.; Ge, J.; Fang, Y. *Langmuir* **2013**, *29*, 15433.
(10) Das, R.; Alonso, J.; Nemati Porshokouh, Z.; Kalappattil, V.; Torres, D.; Phan, M.-H.; Garaio, E.; García, J. Á.; Sanchez Llamazares, J. L.; Srikanth, H. *J. Phys. Chem. C* **2016**, *120*, 10086.
(11) Wang, J.; Chen, Q.; Zeng, C.; Hou, B. *Adv. Mater.* **2004**, *16*, 137.
(12) Zeng, Y.; Hao, R.; Xing, B.; Hou, Y.; Xu, Z. *Chem. Comm.* **2010**, *46*, 3920.
(13) Xu, W.; Wang, M.; Li, Z.; Wang, X.; Wang, Y.; Xing, M.; Yin, Y. *Nano Lett.* **2017**, *17*, 2713.
(14) Yang, Y.; Liu, X.; Lv, Y.; Herng, T. S.; Xu, X.; Xia, W.; Zhang, T.; Fang, J.; Xiao, W.; Ding, J. *Adv. Funct. Mater.* **2015**, **25**, 812.
(15) Mehdaoui, B.; Meffre, A.; Carrey, J.; Lachaize, S.; Lacroix, L.-M.; Gougeon, M.; Chaudret, B.; Respaud, M. *Adv. Funct. Mater.* **2011**, *21*, 4573.


## Iron Oxide Nanoparticles

| Name | Dimensions | Purity & Concentration | Form | Cat. No. |
|---|---|---|---|---|
| Iron | avg. part. size 25 nm | 99.5% trace metals basis | nanopowder | **746827-5G** |
| | avg. part. size 25 nm | 99.5% trace metals basis | nanopowder | **746835-5G** |
| | particle size 35 - 45 nm | 99.5% trace metals basis | nanopowder | **746843-5G** |
| | particle size 40 - 60 nm | 99% trace metals basis | nanopowder | **746851-25G** |
| | particle size 60 - 80 nm | ≥99% trace metals basis | nanopowder | **746878-25G** |
| | particle size <100 nm | 99.5% trace metals basis in mineral oil | dispersion | **513423-5G** |
| Iron oxide(II,III), magnetic nanoparticles solution | avg. part. size 5 nm | 5 mg/mL in toluene | solution | **700320-5ML** |
| | avg. part. size 10 nm | 5 mg/mL in toluene | solution | **700312-5ML** |
| | avg. part. size 20 nm | 5 mg/mL in toluene | solution | **700304-5ML** |
| | avg. part. size 5 nm | 5 mg/mL in $H_2O$ | dispersion | **725331-5ML** |
| | avg. part. size 10 nm | 5 mg/mL in $H_2O$ | dispersion | **725358-5ML** |
| | avg. part. size 20 nm | 5 mg/mL in $H_2O$ | dispersion | **725366-5ML** |
| Iron(III) oxide | particle size <50 nm (BET) | - | nanopowder | **544884-5G** **544884-25G** |
| Iron(III) oxide, dispersion | particle size ≤110 nm | 15 wt. % in ethanol | nanoparticles | **720712-100G** |
| | particle size ≤110 nm | 20 wt. % in $H_2O$ | nanoparticles | **720704-100G** |
| Iron oxide hydroxide | <5 nm (DLS) | 99.5% trace metals basis 20 wt. % in water | dispersion | **796093-100ML** |
| Iron oxide (II,III), nanoparticles | avg. part. size 10 nm (TEM) | 5 mg/mL in chloroform | dispersion | **900084-5ML** |
| | avg. part. size 25 nm (TEM) | 5 mg/mL in $H_2O$ | dispersion | **900042-5ML** |
| | avg. part. size 30 nm (TEM) | 5 mg/mL in $H_2O$ | dispersion | **900062-5ML** |

## Functionalized Iron Oxide Nanoparticles

| Functional Group | Form | Composition | Particle Size (nm) | Cat. No. |
|---|---|---|---|---|
| amine | dispersion | 1 mg/mL in $H_2O$ | avg. part. size 15 (TEM) | **900199-10ML** |
| | dispersion | 1 mg/mL in $H_2O$ | avg. part. size 25 (TEM) | **900028-10ML** |
| | dispersion | Fe 1 mg/mL in $H_2O$ | avg. part. size 5 (TEM) | **747343-10ML** |
| | dispersion | Fe 1 mg/mL in $H_2O$ | avg. part. size 10 (TEM) | **747300-10ML** |
| | dispersion | Fe 1 mg/mL in $H_2O$ | avg. part. size 30 (TEM) | **747327-10ML** |
| biotin | dispersion | 1 mg/mL (in 10 mM PBS buffer) | avg. part. size 15 (TMS) | **900037-1ML** |
| | dispersion | Fe 1 mg/mL in $H_2O$ | avg. part. size 5 (TEM) | **747416-1ML** |
| | dispersion in $H_2O$ | Fe 1 mg/mL | particle size 10 (TEM) | **747424-1ML** |
| | dispersion | Fe 1 mg/mL in $H_2O$ | avg. part. size 30 (TEM) | **747432-1ML** |
| carboxylic acid | dispersion | 5 mg/mL in $H_2O$ | avg. part. size 15 (TEM) | **900200-2ML** |
| | dispersion | 5 mg/mL in $H_2O$ | avg. part. size 25 (TEM) | **900201-2ML** |
| | dispersion | Fe 5 mg/mL in $H_2O$ | avg. part. size 10 (TEM) | **747254-2ML** |
| | dispersion | Fe 5 mg/mL in $H_2O$ | avg. part. size 5 (TEM) | **797146-2ML** |
| | dispersion | - | avg. part. size 30 (TEM) | **747335-2ML** |
| dextran | dispersion | 10 mg/mL in $H_2O$ | avg. part. size 5 (TEM) | **900147-2ML** |
| NHS ester | powder | Fe ~ 1.25 % (w/w) | avg. part. size 5 (TEM) | **747440-1G** |
| | powder | Fe ~ 1.25 % (w/w) | avg. part. size 10 (TEM) | **747459-1G** |
| | powder | Fe ~ 1.25 % (w/w) | avg. part. size 30 (TEM) | **747467-1G** |
| | powder | - | avg. part. size 15 (TEM) | **900041-1G** |
| | powder | - | 25 | **900034-1G** |
| oleic acid | dispersion | 5 mg/mL in chloroform | avg. part. size 5 (TEM) | **900082-5ML** |
| | dispersion | 5 mg/mL in chloroform | avg. part. size 15 (TEM) | **900083-5ML** |
| | dispersion | 5 mg/mL in chloroform | avg. part. size 20 (TEM) | **900088-5ML** |
| | dispersion | 5 mg/mL in chloroform | avg. part. size 25 (TEM) | **900089-5ML** |
| | dispersion | 5 mg/mL in chloroform | avg. part. size 30 (TEM) | **900090-5ML** |
| | dispersion | 5 mg/mL in toluene | avg. part. size 15 (TEM) | **900063-5ML** |
| | dispersion | 5 mg/mL in toluene | avg. part. size 25 (TEM) | **900064-5ML** |
| | dispersion | 5 mg/mL in toluene | avg. part. size 30 (TEM) | **900081-5ML** |
| PEG | dispersion | 1 mg/mL in $H_2O$ | avg. part. size 15 (TEM) | **900026-10ML** |
| | dispersion | 1 mg/mL in $H_2O$ | avg. part. size 25 (TEM) | **900027-10ML** |
| | dispersion | Fe 1 mg/mL in $H_2O$ | avg. part. size 10 (TEM) | **747319-10ML** |
| | dispersion | Fe 1 mg/mL in $H_2O$ | avg. part. size 30 (TEM) | **747408-10ML** |
| | dispersion | Fe 1 mg/mL in $H_2O$ | avg. part. size 5 (TEM) | **747319-10ML** |
| rhodamine B | dispersion | 1 mg/mL in $H_2O$ | avg. part. size 10 (TEM) | **900146-2ML** |
| streptavidin | dispersion | 1 mg/mL in $H_2O$ | avg. part. size 10 (TEM) | **900091-1ML** |
| | dispersion | 1 mg/mL in $H_2O$ | avg. part. size 15 (TEM) | **900092-1ML** |
| | dispersion | 1 mg/mL in $H_2O$ | avg. part. size 20 (TEM) | **900093-1ML** |
| | dispersion | 1 mg/mL in $H_2O$ | avg. part. size 25 (TEM) | **900094-1ML** |
| | dispersion | 1 mg/mL in $H_2O$ | avg. part. size 30 (TEM) | **900148-1ML** |
| - | dispersion | 5 mg/mL in $H_2O$ | avg. part. size 15 (TEM) | **900043-5ML** |

## Poly(acrylic acid)

| Name | Molecular Weight | Viscosity (cP) | Cat. No. |
|---|---|---|---|
| Poly(acrylic acid) | - | 350-700 | **900338-250G** |
| | average $M_w$ 1800 | ≤2000 | **323667-5G**<br>**323667-100G**<br>**323667-250G** |
| | average $M_v$ ~450,000 | 350-2500 | **181285-5G**<br>**181285-100G**<br>**181285-250G** |
| | average $M_v$ ~1,250,000 | 800-11,000 | **306215-5G**<br>**306215-100G**<br>**306215-250G** |
| | average $M_v$ ~3,000,000 | 30,000-40,000 | **306223-100G**<br>**306223-250G** |
| | average $M_v$ ~4,000,000 | 40,000-60,000 | **306231-5G**<br>**306231-100G** |

## Poly(acrylic acid) Solution

| Name | Molecular Weight | Concentration (wt. %) | Cat. No. |
|---|---|---|---|
| Poly(acrylic acid) solution | average $M_w$ ~2,000 | 50 in $H_2O$ | **535931-100G** |
| | average $M_w$ ~100,000 | 35 in $H_2O$ | **523925-100ML**<br>**523925-500ML** |
| | average $M_w$ ~250,000 | 35 in $H_2O$ | **416002-5ML**<br>**416002-250ML**<br>**416002-500ML** |

## Poly(acrylic acid sodium salt)

| Name | Molecular Weight | Cat. No. |
|---|---|---|
| Poly(acrylic acid sodium salt) | average $M_w$ ~2,100 | **420344-100G**<br>**420344-500G** |
| | average $M_w$ ~5,100 by GPC | **447013-100G**<br>**447013-500G** |

## Poly(acrylic acid sodium salt) Solution

| Name | Molecular Weight | Concentration (wt. %) | Cat. No. |
|---|---|---|---|
| Poly(acrylic acid, sodium salt) solution | average $M_w$ ~1,200 | 45 in $H_2O$ | **416010-100ML**<br>**416010-500ML** |
| | average $M_w$ ~8,000 | 45 in $H_2O$ | **416029-100ML**<br>**416029-500ML** |
| | average $M_w$ ~15,000 | 35 in $H_2O$ | **416037-100ML**<br>**416037-500ML** |

# Beyond pure

Ultra-high purity metals, salts, and oxides are essential in creating advanced materials. Explore the breadth of our portfolio's materials with purity of 99.999% or higher for applications such as:

- Photovoltaics
- Phosphor materials
- Nanoparticle synthesis
- Magnetic memory
- Biomedical applications
- Electronic devices

| Product Description | Cat. No. |
|---|---|
| **Metals** | |
| Aluminum, wire, diam. 1.0 mm, 99.999% trace metals basis | **266558** |
| Antimony, beads, 1-5 mm, low oxide, 99.999% trace metals basis | **452343** |
| Bismuth, pieces, 1-12 mm, 99.999% trace metals basis | **556130** |
| Copper, powder, 99.999% trace metals basis | **203122** |
| Gallium, 99.9995% trace metals basis | **203319** |
| Germanium, chips, 99.999% trace metals basis | **203343** |
| Gold, beads, 1-6 mm, 99.999% trace metals basis | **326542** |
| Indium, beads, diam. 2-5 mm, 99.999% trace metals basis | **264113** |
| Selenium, pellets, <5 mm particle size, ≥99.999% trace metals basis | **204307** |
| Silicon, powder, −60 mesh, 99.999% trace metals basis | **267414** |
| Zinc, foil, thickness 0.25 mm, 99.999% trace metals basis | **267619** |
| **Oxides** | |
| Bismuth(III) oxide, powder, 99.999% trace metals basis | **202827** |
| Copper(II) oxide, 99.999% trace metals basis | **203130** |
| Europium(III) oxide, 99.999% trace metals basis | **323543** |
| Germanium(IV) oxide, powder, 99.999% trace metals basis | **483001** |
| Holmium(III) oxide, powder, 99.999% trace metals basis | **229679** |
| Iron(III) oxide, ≥99.995% trace metals basis | **529311** |
| Lanthanum(III) oxide, 99.999% trace metals basis | **203556** |
| Lead(II) oxide, 99.999% trace metals basis | **203610** |
| Mercury(II) oxide, 99.999% trace metals basis | **203793** |
| Zinc oxide, 99.999% trace metals basis | **204951** |

| Product Description | Cat. No. |
|---|---|
| **Salts** | |
| Aluminum chloride, anhydrous, powder, 99.999% trace metals basis | **563919** |
| Ammonium acetate, 99.999% trace metals basis | **372331** |
| Barium chloride dihydrate, ≥99.999% trace metals basis | **529591** |
| Cesium chloride, ≥99.999% trace metals basis | **203025** |
| Copper(I) bromide, 99.999% trace metals basis | **254185** |
| Copper(II) nitrate hydrate, 99.999% trace metals basis | **229636** |
| Gallium(III) chloride, beads, anhydrous, ≥99.999% trace metals basis | **427128** |
| Gold(III) chloride hydrate, 99.995% trace metals basis | **254169** |
| Indium(III) chloride, 99.999% trace metals basis | **203440** |
| Lanthanum(III) nitrate hexahydrate, 99.999% trace metals basis | **203548** |
| Lead(II) bromide, 99.999% trace metals basis | **398853** |
| Lead(II) iodide, beads, −10 mesh, 99.999% trace metals basis | **554359** |
| Silver nitrate, 99.9999% trace metals basis | **204390** |
| Sodium chloride, 99.999% trace metals basis | **204439** |
| Sodium nitrite, 99.999% trace metals basis | **563218** |
| Zinc nitrate hydrate, 99.999% trace metals basis | **230006** |

For a complete list of ultra-high purity products, visit **SigmaAldrich.com/uhp**

# Magnetic-Plasmonic Hybrid Nanobeads Designed for Imaging and Isolation of Cellular Organelles


Mari Takahashi and Shinya Maenosono*

School of Materials Science, Japan Advanced Institute of Science and Technology
1-1 Asahidai, Nomi, Ishikawa 923-1292, Japan
*E-mail: shinya@jaist.ac.jp

## Introduction

Cells take up extracellular solute and proteins/lipids on the plasma membranes by endocytosis and package them into endocytic vesicles. The internalized materials are then either delivered to lysosomes for degradation or recycled back to the plasma membrane for reuse. The endocytosis process is fundamental to many other biological processes, including nutrition uptake, regulation of mitogenic signaling, cell differentiation and locomotion, and immune response. Moreover, some pathogens such as viruses and bacteria exploit endocytosis to invade host cells. It follows that the study of the molecular machinery that regulates endocytosis and characterization of the protein/lipid components of endocytic vesicles is essential for improving our fundamental understanding of cell biology and pathology. Recently, magnetic separation of endocytic vesicles/endosomes has been reported by several groups.[1,2] These magnetic separation techniques enable recovery of purified and undamaged target material, and serve as useful alternatives to other techniques such as ultracentrifugation and density-gradient separation.[3]

Immunomagnetic isolation separates cells and subcellular organelles using magnetic beads coupled with cell-surface or organelle-specific antibodies. In contrast to traditional purification methods using ultracentrifugation, immunomagnetic isolation is rapid and gentle, protecting the integrity of isolated cells and organelles. Magnetic beads have been used to isolate endocytic organelles—such as early and late endosomes—through endocytosis of beads into the lumen of organelles. We have previously fabricated ultrasmall magnetic beads with an Ag/FeCo/Ag core/shell/shell structure.[4] Although these magnetic probes have a magnetically inert Ag core (mean size 10 nm), these beads still facilitate separation. Further, the Ag core enables visualization of the bead using a microscope. The intrinsic optical properties and localized surface plasmon resonance of Au and Ag metallic nanoparticles has led to their use in cell imaging.[5,6] The combination of these materials enables magnetic beads with plasmonic properties; hereafter they are referred to as magnetic-plasmonic hybrid nanobeads (MPNBs).

## Brief History of MPNBs

The superparamagnetic properties of magnetic nanoparticles enable their use in applications such as magnetic hyperthermia, magnetic resonance imaging, contrast agents, magnetic separation, and magnetic drug delivery. In addition, the plasmonic properties of metal nanoparticles enable technologies such as sensing, imaging and photothermal therapy. Therefore, combining these properties into a single nanostructure offers more highly diverse applications than when applying either superparamagnetic or plasmonic properties alone. Several types of MPNBs have been reported including Au-$Fe_3O_4$ heterostructured MPNBs,[7] Co/Au core/shell MPNBs,[8] and FePt-Au heterostructured MPNBs.[9] **Table 1** overviews MPNBs with various functionalities stemming from individual magnetic and plasmonic components.

Assorted liquid-phase synthetic methods have been investigated to obtain different types of MPNBs such as alloy, core/shell, core/satellite, or heterodumbbell structures with different combinations of magnetic and plasmonic materials. In the following section typical wet-chemical synthesis methods for MPNBs are reviewed.

**Table 1.** MPNBs with different functionalities

| Magnetic Component Functionality | Plasmonicc Component Functionality | References |
|---|---|---|
| Magnetic manipulation (separation/delivery) | Optical imaging | 4,10-13 |
| | Photothermal therapy | 11,14,15 |
| | Sensing | 16-19 |
| Magnetic hyperthermia | Photothermal therapy | 20-24 |
| | Sensing | 20,25 |
| Magnetic resonance imaging | Optical imaging | 13,26-29 |
| | Photothermal therapy | 26,27,30,31 |
| | Sensing | 18,25 |

### Aqueous Reduction Method

In the aqueous reduction method, MPNBs are typically synthesized by sequential reductions of plasmonic and magnetic precursors with a reducing agent in an aqueous solvent. Santhi et al. synthesized Ag-Ni alloy MPNBs by adding a reducing agent to aqueous solution containing Ag and Ni precursors.[32] Wang et al. reported a composition-tunable synthesis method of Co/Ag core/shell MPNBs by injecting Ag precursors into aqueous solution containing Co precursors and reducing agents.[33] Kostevšek et al. reported FePt/$SiO_2$/Au core/shell/shell MPNBs using a combination of three methods: the reduction method for FePt core formation, the sol-gel method for $SiO_2$ shell formation and the seed-mediated growth method for Au shell formation.[34]

### Heat-up Method

Among organic synthesis methods, the heat-up method is facile and reliable for synthesizing uniform MPNBs in a controlled fashion. Typically, metal precursors and stabilizers are dissolved in organic solvent with or without reducing agents. Then, the reaction mixture is heated to high temperature to promote the reduction/decomposition reaction. By precisely controlling the reaction temperature, various types of uniform MPNBs can be synthesized. For example, Yu et al. synthesized dumbbell-like Au-$Fe_3O_4$ MPNBs by using the heat-up method.[35] Peng and coworkers synthesized Au/Ni and Ag/Ni core/shell MPNBs using the heat-up method in combination with a sequential reduction of precursors.[36,37] As an example of a seed-mediated growth method, which is a form of the heat-up method, Wang et al. synthesized $Fe_3O_4$/Au core/shell MPNBs using a modified polyol reduction (polyol method) of Au precursors onto preformed iron oxide nanoparticles.[38]

### Hot Injection Method

Hot injection is another organic synthesis method used to obtain well-defined uniform MPNBs. Typically, a stock solution of metal precursor(s) is injected into organic solvent containing stabilizers at high temperature. This method enables decoupling nucleation and growth of nanoparticles; thus, wider varieties of uniform MPNBs can be synthesized. Bao et al. synthesized Co/Au core/shell MPNBs by a two-step injection method in which Co cores were formed, followed by Au shell formation onto the cores.[39] Peng et al. synthesized dumbbell-like Ag-$Fe_3O_4$ MPNBs by injecting Ag precursors into a solution containing Fe/$Fe_xO_y$ core/shell magnetic nanoparticles.[40] Mohan et al. synthesized $Au_{100-x-y}Fe_xPt_y$ ternary alloy MPNBs by injecting Au and Fe precursors into a reaction solution containing Pt precursors.[41]

### Solvothermal Method

The solvothermal method is another important method for preparing MPNBs in which chemicals are reacted under extreme conditions such as middle-high temperature (100–500°C) and pressure (1–10,000 atm). In a typical solvothermal method, the reaction mixture containing metal precursors and stabilizers are heated with a Teflon-lined stainless-steel autoclave. This method enables the use of the enhanced solubility of metal precursors by exceeding the boiling point of a solvent under an elevated pressure. Zhai et al. reported a size-tuned solvothermal synthesis of Ag/$Fe_3O_4$ core/satellite nanostructures.[42] Shan et al. also synthesized Ag-$Fe_3O_4$ nanocomposites using the solvothermal method.[43] In their synthesis, they tuned magnetic and plasmonic properties by changing the input molar ratio of Ag and Fe precursors.

## Synthesis and Characterization of MPNBs

Ag/FeCo/Ag core/shell/shell MPNBs were synthesized by combining the hot injection and polyol methods.[4,44] First, silver nitrate ($AgNO_3$) (**Cat. No. 204390**), 1,2-hexadecanediol (**Cat. No. 213748**), oleic acid (**Cat. No. O1008**), oleylamine (OLA) (**Cat. No. O7805**), and tetraethylene glycol (**Cat. No. 110175**) were combined. The reaction mixture was degassed with Argon (**Cat. No. 295000**) for 5 minutes at room temperature with vigorous stirring, then heated to 100°C for 10 minutes to remove volatile substances. The temperature was increased to 170°C and a solution of iron(III) acetylacetonate [$Fe(acac)_3$] (**Cat. No. 517003**) and cobalt(II) acetylacetonate [$Co(acac)_2$] (**Cat. No. 227129**) in OLA and toluene (**Cat. No. 244511**) was added. The temperature was increased to 250°C, and a solution of $AgNO_3$ in OLA and toluene was added to form the Ag outer shell. The temperature was reduced to

230°C for 15 min and then to room temperature. Acetone (**Cat. No. 179124**) was added and the MPNBs were centrifuged and subsequently redispersed in hexane (**Cat. No. 296090**). All chemicals were purchased from Sigma-Aldrich and used as received. The MPNBs were then modified with thiolated ε-poly-l-lysine (PLL-SH). The MPNBs were characterized using transmission electron microscopy (TEM), high-resolution TEM (HRTEM), scanning TEM equipped with a high-angle annular dark-field (STEM-HAADF) detector, energy-dispersive X-ray spectroscopy (EDS) elemental mapping, X-ray photoelectron spectroscopy (XPS), X-ray diffraction (XRD), inductively coupled plasma optical emission spectroscopy (ICP-OES), superconducting quantum interference device (SQUID) magnetometry, and ultraviolet-visible spectroscopy (UV-vis).

## Morphology and Properties of MPNBs

**Figure 1** shows TEM and STEM images of as-synthesized Ag/FeCo/Ag MPNBs, these MPNBs were spherical and showed a distinct core-shell structure. The average diameter of MPNBs was calculated to be ~15 nm.[4,44-47] It is evident from these images that the MPNBs have a distinct Ag core and FeCo shell. **Figure 1H** shows the EDS line profile (yellow line in **Figure 1G**). The Ag signal clearly increased at the edge of the MPNBs confirming the presence of a thin Ag outer shell.

**Figure 2** shows Fe 2p and Co 2p XPS spectra for the MPNBs.[45] The atomic ratio between Fe and Co was determined to be Fe:Co = 67:33. In contrast, the Fe:Co composition measured by ICP-OES was near equiatomic. This discrepancy is attributed to a composition gradient within the FeCo shell, with Co being rich near the Ag core, while Fe is rich on the surface of the FeCo shell. The relative oxidation state proportions of each species were $Fe^0/Fe^{2+}/Fe^{3+}$ = 15:56:29 and $Co^0/Co^{2+}/Co^{3+}$ = 23:47:30. X-ray diffraction (XRD) analysis of the MPNBs revealed that FeCo and $Co_xFe_{1-x}O$ phases are simultaneously present.[45] Considering all of the data together, it can be said that the surface of the FeCo shell is likely to oxidize to form the $Co_xFe_{1-x}O$ cobalt-wüstite layer. In order to confirm this supposition, the magnetic properties of the MPNBs were examined using a superconducting quantum interference device (SQUID) magnetometer. **Figure 3** shows magnetization (*M-H*) curves recorded at T = 5 K, after zero-field cooling (ZFC) and field cooling (FC) in a 1 T magnetic field. As shown in **Figure 3**, the hysteresis loop after the FC procedure was shifted along the field axis in the negative direction to the cooling field, indicating the presence of exchange bias. This result also suggests the existence of an interface between ferromagnetic (FeCo) layer and antiferromagnetic ($Co_xFe_{1-x}O$) layer within the shell.[45]

Based on the STEM, XPS, XRD, and SQUID analyses, we concluded that the detailed structure of a single MPNB is as shown in **Figure 4**. We also note that the magneto-optical properties of the MPNBs were found to be modified with an enhancement of the Faraday rotation and ellipticity of 5× compared with the pure FeCo nanoparticles.[48] The modifications are mainly due to the plasmonic core in the hybrid structure and the strong coupling between the magnetic and plasmonic materials. Such strong coupling was achieved owing to the bead morphology (i.e. the plasmonic structure at the core).

We elucidated the formation mechanism of Ag/FeCo/Ag MPNBs was a combination of two well known phenomena: (1) competition between size focusing and Ostwald ripening and (2) size-dependent catalysis of Ag nanoparticles. The injection of Ag precursor causes size focusing of the Ag cores such that the monodispersed cores are larger than the critical size. Consequently, electrons are transferred from the polyol to the Ag cores and the Ag cores to the Co or Fe ions, and then the FeCo shells are formed uniformly on the Ag cores. During FeCo shell formation, Ag atoms are simultaneously incorporated into the FeCo shell, and the surface segregation of Ag takes place spontaneously, resulting in formation of an Ag outer shell.[44]

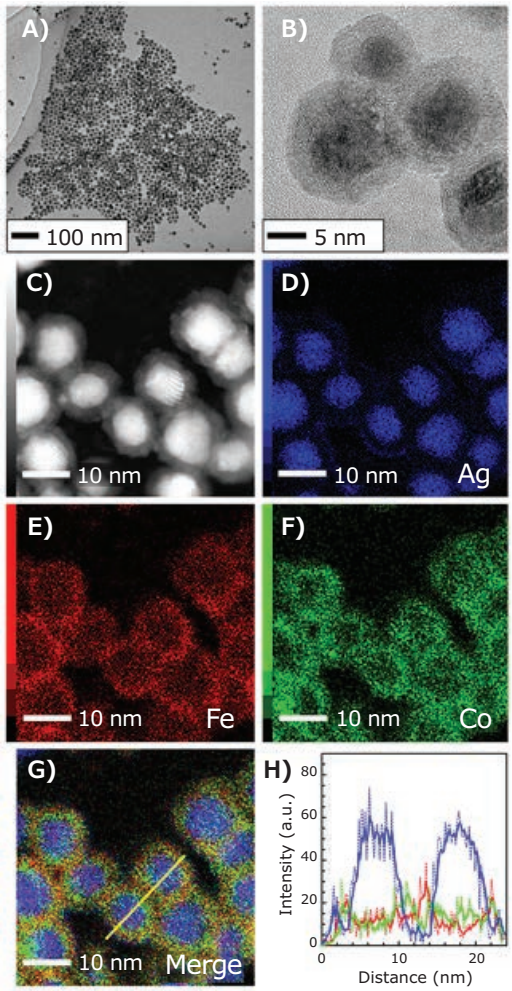


**Figure 1.** **A**) TEM, **B**) HRTEM, and **C**) STEM-HAADF images of MPNBs. **D**) Ag L, **E**) Fe K, **F**) Co K, and **G**) merged images of EDS elemental mapping images for MPNBs. **H**) EDS line profile along the yellow line in **G**). Reprinted with permission from reference 47, copyright 2017 American Chemical Society.

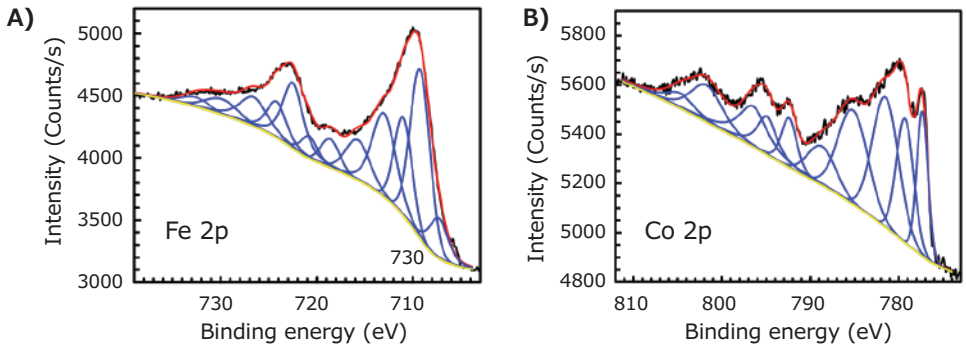


**Figure 2.** A) Fe 2p and B) Co 2p XPS spectra for MPNBs. Black, yellow, blue, and red curves represent raw data, Shirley background, deconvolved peaks, and the sum of all components, respectively. Reprinted with permission from reference 45, copyright 2016 Elsevier.

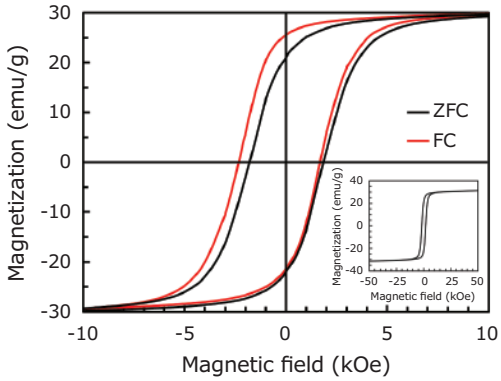


**Figure 3.** *M-H* curves in the range of -10 to 10 kOe recorded at T = 5 K, after ZFC (black) and FC (red) procedures. The inset shows the entire *M-H* curve after the ZFC procedure. Reprinted with permission from reference 45, copyright 2016 Elsevier.

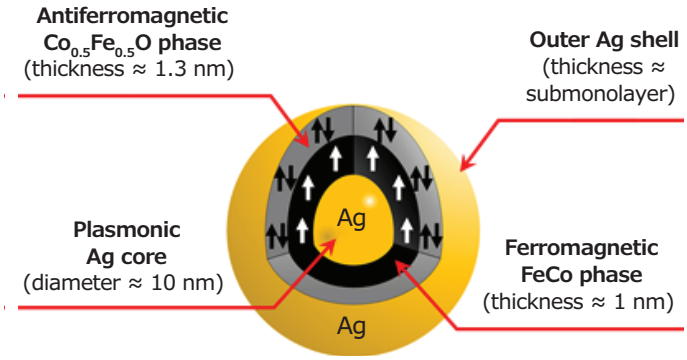


**Figure 4.** Illustration of a single MPNB showing its internal structure.

## Imaging and Isolation of Autophagosomes Using MPNBs

Autophagosomes were chosen as target organelles. It has been reported that micrometer-sized polystyrene beads lipofected into mammalian cells are delivered into early endosomes causing damage and inducing xenophagy, whereby damaged endosomes are engulfed by autophagosomes.[49,50] Although autophagosomes can engulf micrometer-sized beads,[49] we used MPNBs to demonstrate the ability of MPNBs to magnetically isolate subcellular organelles.

PLL-SH-modified MPNBs were transfected into COS-1 cells by lipofection.[47] Cells were then fixed, stained for Vps26 (early endosomal marker protein) or LC3 (autophagosomal marker protein), and examined by confocal laser scanning microscopy (CLSM). Thirty minutes after transfection, the MPNBs were partially co-localized with Vps26, but not with LC3 (**Figure 5A–C**). One hour after lipofection, some MPNB-positive structures surrounded by LC3 emerged (**Figure 5D**). These structures were mostly evident 2 and 4 h after lipofection (**Figures 5E and F**). This indicated that the MPNBs were first delivered into early endosomes, and then targeted to autophagosomes. Imaging of MPNBs was achieved using plasmon scattering.

The MPNB lipofected cells were detached from the culture dish and homogenized. The resultant cell lysates were magnetically separated using an autoMACS Pro Separator (Miltenyi Biotec, Germany). The magnetically separated fraction (MS) was eluted from the column, spun briefly, and resuspended in phosphate buffered saline (PBS) (**Cat. No. P4244**) (**Figure 6A**). The cell lysate and MS were subjected to SDS-PAGE and blotted for LC3, transferrin receptor (TfnR, an endosomal protein), lysosomal-associate membrane-2 (LAMP2, a lysosomal protein), and glyceraldehyde 3-phosphate dehydrogenase (GAPDH, a cytosolic protein). As shown in **Figure 6B**, at time 0, no proteins of interest were detected in the MS. After 15 min, LC3-II (a membrane-bound form of LC3), tumor necrosis factor receptor (TfnR), and LAMP2, but not GAPDH, were detected in the MS. The levels of LC3-II and LAMP2 increased up to 8 h, whereas that of TfnR plateaued after 2 h. Throughout the separation experiments, no GAPDH or LC3-I (a cytosolic form of LC3) was detected in the MS. These results indicated that at early time points ($0.5<t<2$ h, ($t$ is incubation time)) mainly autophagosomes were isolated, and in contrast, at later time points ($t>2$ h), autophagolysosomes were isolated.[47]

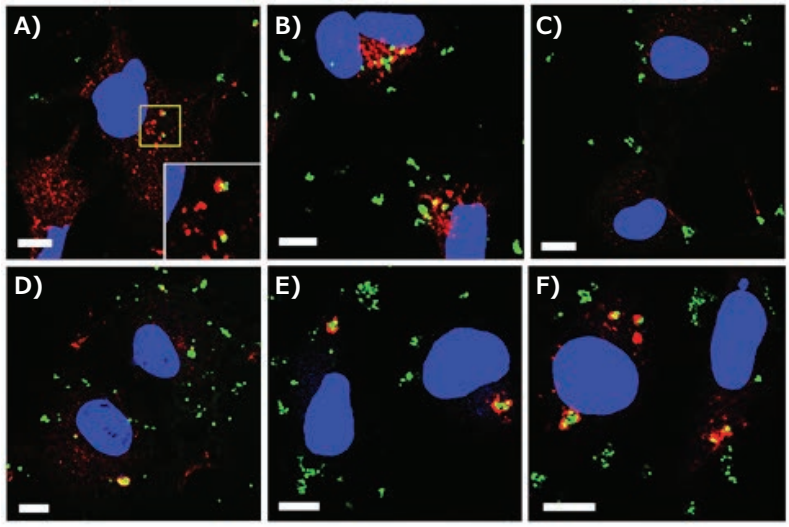


**Figure 5.** CLSM images of MPNB-transfected COS-1 cells after incubation for **A**) 30 min and **B**) 1 h for Vps26 staining, and **C**) 30 min, **D**) 1 h, **E**) 2 h, and **F**) 4 h for LC3 staining. Blue and green represent nuclei and MPNBs, respectively. Red represents Vps26 (**A**,**B**) or LC3 (**C**–**F**). Scale bars correspond to 10 μm. The inset shown at the bottom right of (**A**) is a magnified view of the region enclosed by the yellow line in (**A**). Reprinted with permission from reference 47, copyright 2017 American Chemical Society.

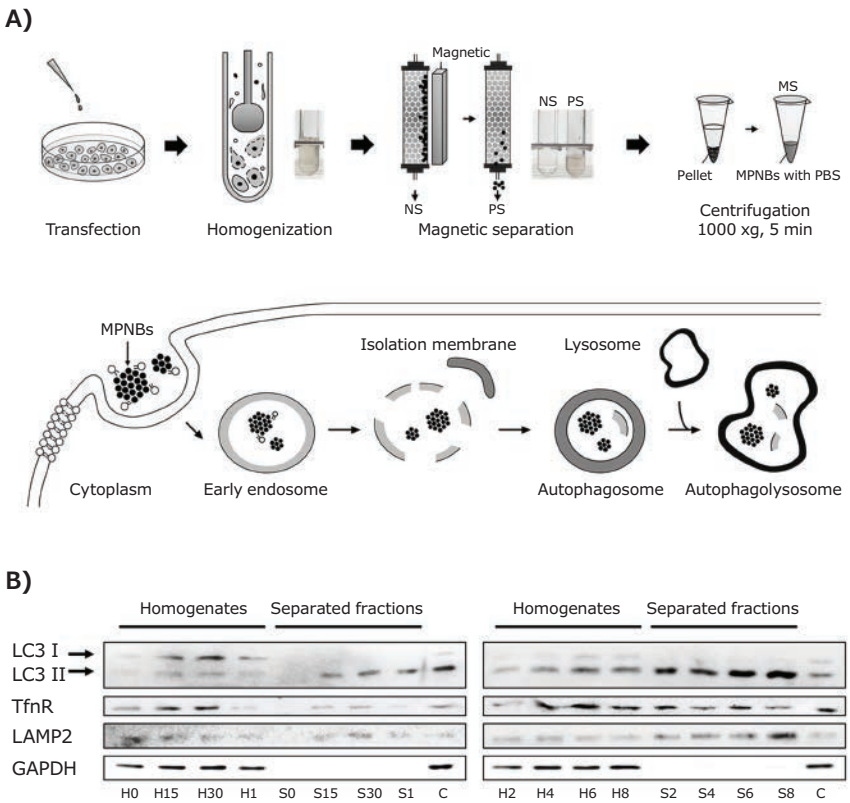


**Figure 6.** Magnetic separation scheme and western blotting results. **A**) Schematic illustrations of (**top**) the magnetic separation protocol and (**bottom**) the change in the localization of hybrid nanoparticles in a cell. **B**) The incubation time dependence of the presence of marker proteins in the homogenate (designated H) and the separated fractions (MS, designated S). C is a control in which the transfection reagent was present but nanoparticles were absent. The number added after the initial of the sample (H or S) denotes the incubation time, that is, 0, 15, and 30 correspond to 0, 15, and 30 min incubations, respectively, while 1, 2, 4, 6, and 8 correspond to 1, 2, 4, 6, and 8 h incubations, respectively. Reprinted with permission from reference 47, copyright 2017 American Chemical Society.

## Conclusion

Monodispersed Ag/FeCo/Ag core/shell/shell MPNBs were synthesized and transfected into COS-1 cells by lipofection. After incubation the localization of MPNBs in cells was visualized by confocal laser scanning microscopy (CLSM) using the plasmon scattering of the Ag cores. The MPNBs reached early endosomes within 30 min, and subsequently became positive for LC3. Autophagosomes containing MPNBs were then successfully isolated by magnetic separation. This process took ~30 min after cell lysis, providing a rapid method for isolating autophagosomes. The ability of MPNBs to magnetically isolate cellular organelles was clearly demonstrated and is promising for isolation of other organelles such as endosome-related organelles, the trans-Golgi network, and clathrin-coated vesicles. By enabling on-demand isolation of cellular organelles, developing MPNBs to identify proteins on/in the organelles, and analyzing the function of these proteins, it will become possible to offer new insights in both biology and clinical medicine.

## Acknowledgements

This work was supported by a Grant-in-Aid for Scientific Research, Grant nos. 26600053 and 15J10127. We are indebted to Prof. Tomohiko Taguchi and Assist. Prof. Kojiro Mukai (Graduate School of Life Sciences, Tohoku University, Japan) for their longtime collaboration on cell biology issues. We thank Prof. Masahiro Takakura (Department of Obstetrics and Gynecology, Kanazawa Medical University, Japan) and Dr. Takeo Matsumoto (Graduate School of Medical Sciences, Kanazawa University, Japan) for their assistance in magnetic separation experiments. We also thank Prof. Kazuaki Matsumura, Prof. Yuichi Hiratsuka, Ms. Keiko Kawamoto, and Ms. Chiharu Tatsumi of Japan Advanced Institute of Science and Technology (JAIST) for their assistance in cell experiments. We are grateful to Assist. Prof. Shigetaka Nakamura and Prof. Kenzo Fujimoto of JAIST for their support in performing chemiluminescence detection of western blots. We are also obliged to Prof. Satoshi Waguri (Department of Anatomy and Histology, Fukushima Medical University, Japan) for his valuable comments on TEM images of cell organelles, and Dr. Alberto López-Ortega (Department of Applied Physics, University of Castilla-La Mancha, Spain) and Prof. Paolo Vavassori (CIC nanoGUNE, Spain) for collaborative research on magneto-optical effects of the MPNBs. We are also grateful to Dr. Priyank Mohan (JAIST), Dr. Derrick Mott (IMRAM, Tohoku University, Japan), and Mr. Koichi Higashimine (JAIST) for their support over the years.

## References

(1) Wittrup, A.; Zhang, S. H.; Svensson, K. J.; Kucharzewska, P.; Johansson, M. C.; Mörgelin, M.; Belting, M. *Proc. Natl. Acad. Sci. USA* **2010**, *107*, 13342–13347.
(2) Nakamura, N.; Lill, J. R.; Phung, Q.; Jiang, Z.; Bakalarski, C.; de Mazière, A.; Klumperman, J.; Schlatter, M.; Delamarre, L.; Mellman, I. *Nature* **2014**, *509*, 240–244.
(3) Tauro, B. J.; Greening, D. W.; Mathias, R. A.; Ji, H.; Mathivanan, S.; Scott, A. M.; Simpson, R. J. *Methods* **2012**, *56*, 293–304.
(4) Takahashi, M.; Mohan, P.; Nakade, A.; Higashimine, K.; Mott, D.; Hamada, T.; Matsumura, K.; Taguchi, T.; Maenosono, S. *Langmuir* **2015**, *31*, 2228–2236.
(5) Wang, J.; Yu, X.; Boriskina, S.V.; Reinhard, B.M. *Nano Lett.* **2012**, *12*, 3231–3237.
(6) Wang, H.; Shen, J.; Li, Y.; Wei, Z.; Cao, G.; Gai, Z.; Hong, K.; Banerjee, P.; Zhou, S. *ACS Appl. Mater. Interfaces* **2013**, *5*, 9446–9453.
(7) Lee, Y.; Garcia, M. A.; Huls N. A. F.; Sun, S. *Angew. Chem. Int. Ed.* **2010**, *49*, 1271–1274.
(8) Xu, Y. H.; Bai, J.; Wang, J.-P. *J. Magn. Magn. Mater.* **2007**, *311*, 131–134.
(9) Choi, J. S.; Jun, Y.-W.; Yeon, S.-I.; Kim, H. C.; Shin, J.-S.; Cheon, J. *J. Am. Chem. Soc.* **2006**, *128*, 15982–15983.
(10) Wu, C.-H.; Cook, J.; Emelianov, S.; Sokolov, K. *Adv. Funct. Mater.* **2014**, *24*, 6862–6871.
(11) Ohulchanskyy, T. Y.; Kopwitthaya, A.; Jeon, M.; Guo, M.; Law, W.-C.; Furlani, E. P.; Kim, C.; Prasad, P. N. *Nanomedicine* **2013**, *9*, 1192–1202.
(12) Sotiriou, G. A.; Hirt, A. M.; Lozach, P.-Y.; Teleki, A.; Krumeich, F.; Pratsinis, S. E. *Chem. Mater.* **2011**, **23**, 1985–1992.
(13) Huang, L.; Ao, L.; Hu, D.; Wang, W.; Sheng, Z.; Su, W. *Chem. Mater.* **2016**, *28*, 5896–5904.
(14) Fan, Z.; Senapati, D.; Singh, A. K.; Ray, P. C. *Mol. Pharmaceutics* **2013**, *10*, 857–866.
(15) Li, W.-P.; Liao, P.-Y.; Su, C.-H.; Yeh, C.-S. *J. Am. Chem. Soc.* **2014**, *136*, 10062–10075.
(16) Zhou, X.; Xu, W.; Wang, Y.; Kuang, Q.; Shi, Y.; Zhong, L.; Zhang, Q. *J. Phys. Chem. C* **2010**, *114*, 19607–19613.
(17) Wang, J.; Wu, X.; Wang, C.; Rong, Z.; Ding, H.; Li, H.; Li, S.; Shao, N.; Dong, P.; Xiao, R.; Wang, S. *ACS Appl. Mater. Interfaces* **2016**, *8*, 19958–19967.
(18) Carrouée, A.; Allard-Vannier, E.; Même, S.; Szeremeta, F.; Beloeil, J.-C.; Chourpa, I. *Anal. Chem.* **2015**, *87*, 11233–11241.
(19) Zhai, Y.; Zhai, J.; Wang, Y.; Guo, S.; Ren, W.; Dong, S. *J. Phys. Chem. C* **2009**, *113*, 7009–7014.
(20) Lai, J.-J.; Lai, W.-R.; Chen, C.-Y.; Chen, S.-W.; Chiang, C.-L. *J. Magn. Magn. Mater.* **2013**, *331*, 204–207.
(21) Mazuel, F.; Espinosa, A.; Radtke, G.; Bugnet, M.; Neveu, S.; Lalatonne, Y.; Botton, G. A.; Abou-Hassan, A.; Wilhelm, C. *Adv. Funct. Mater.* **2017**, *27*, 1605997.
(22) Das, R.; Rinaldi-Montes, N.; Alonso, J.; Amghouz, Z.; Garaio, E.; García, J. A.; Gorria, P.; Blanco, J. A.; Phan, M. H.; Srikanth, H. *ACS Appl. Mater. Interfaces* **2016**, *8*, 25162–25169.
(23) Balasubramanian, S.; Girija, A. R.; Nagaoka, Y.; Fukuda, T.; Iwai, S.; Kizhikkilot, V.; Kato, K.; Maekawa, T.; Nair, S. D. *RSC Adv.* **2015**, *5*, 25066–25078.
(24) Espinosa, A.; Bugnet, M.; Radtke, G.; Neveu, S.; Botton, G. A.; Wilhelm, C.; Abou-Hassan, A. *Nanoscale* **2015**, *7*, 18872–18877.
(25) Han, Y.; Lei, S.-L.; Lu, J.-H.; He, Y.; Chen, Z.-W.; Ren, L.; Zhou, X. *Mater. Sci. Eng. C* **2016**, *64*, 199–207.
(26) Wang, X.; Liu, H.; Chen, D.; Meng, X.; Liu, T.; Fu, C.; Hao, N.; Zhang, Y.; Wu, X.; Ren, J.; Tang, F. *ACS Appl. Mater. Interfaces* **2013**, *5*, 4966–4971.
(27) Lim, Y. T.; Cho, M. Y.; Kim, J. K.; Hwangbo, S.; Chung, B. H. *ChemBioChem* **2007**, *8*, 2204–2209.
(28) Amendola, V.; Scaramuzza, S.; Litti, L.; Meneghetti, M.; Zuccolotto, G.; Rosato, A.; Nicolato, E.; Marzola, P.; Fracasso, G.; Anselmi, C.; Pinto, M.; Colombatti, M. *Small* **2014**, *10*, 2476–2486.
(29) Xu, C.; Xie, J.; Ho, D.; Wang, C.; Kohler, N.; Walsh, E. G.; Morgan, J. R.; Chin, Y. E.; Sun, S. *Angew. Chem. Int. Ed.* **2008**, *47*, 173–176.
(30) Larson, T. A.; Bankson, J.; Aaron, J.; Sokolov, K. *Nanotechnology* **2007**, *18*, 325101.
(31) Ma, M.; Chen, H.; Chen, Y.; Wang, X.; Chen, F.; Cui, X.; Shi, J. *Biomaterials* **2012**, *33*, 989–998.
(32) Santhi, K.; Thirumal, E.; Karthick, S. N.; Kim, H.-J.; Nidhin, M.; Narayanan, V.; Stephen, A. *J. Nanopart. Res.* **2012**, *14*, 868.
(33) Wang, L.; Clavero, C.; Huba, Z.; Carroll, K. J.; Carpenter, E. E.; Gu, D.; Lukaszew, R. A. *Nano Lett.* **2011**, *11*, 1237–1240.
(34) Kostevšek, N.; Rožman, K. Ž.; Arshad, M. S.; Spreitzer, M.; Kobe, S.; Šturm, S. *J. Phys. Chem. C* **2015**, *119*, 16374–16382.
(35) Yu, H.; Chen, M.; Rice, P. M.; Wang, S. X.; White, R. L.; Sun, S. *Nano Lett.* **2005**, *5*, 379–382.
(36) She, H.; Chen, Y.; Chen, X.; Zhang, K.; Wang, Z.; Peng, D.-L. *J. Mater. Chem.* **2012**, *22*, 2757–2765.
(37) Guo, H.; Chen, Y.; Chen, X.; Wen, R.; Yue, G.-H.; Peng, D.-L. *Nanotechnology* **2011**, *22*, 195604.

(38) Wang, L.; Luo, J.; Fan, Q.; Suzuki, M.; Suzuki, I. S.; Engelhard, M. H.; Lin, Y.; Kim, N.; Wang, J. Q.; Zhong, C.-J. *J. Phys. Chem. B* **2005**, *109*, 21593–21601.
(39) Bao, Y.; Calderon, H.; Krishnan, K. M. *J. Phys. Chem. C* **2007**, *111*, 1941–1944.
(40) Peng, S.; Lei, C.; Ren, Y.; Cook, R. E.; Sun, Y. *Angew. Chem. Int. Ed.* **2011**, *50*, 3158–3163.
(41) Mohan, P.; Takahashi, M.; Higashimine, K.; Mott, D.; Maenosono, S. *Langmuir* **2017**, *33*, 1687–1694.
(42) Zhai, Y.; Han, L.; Wang, P.; Li, G.; Ren, W.; Liu, L.; Wang, E.; Dong, S. *ACS Nano* **2011**, *5*, 8562–8570.
(43) Shan, Y.; Yang, Y.; Cao, Y.; Huang, Z. *RSC Adv.* **2015**, *5*, 102610–102618.
(44) Takahashi, M.; Higashimine, K.; Mohan, P.; Mott, D.; Maenosono, S. *CrystEngComm* **2015**, *17*, 6923–6929.
(45) Takahashi, M.; Mohan, P.; Mott, D.; Maenosono, S. *J. Magn. Magn. Mater.* **2016**, *401*, 339–344.
(46) Takahashi, M.; Mohan, P.; Higashimine, K.; Mott, D.; Maenosono, S. *J. Appl. Phys.* **2016**, *120*, 134301.
(47) Takahashi, M.; Mohan, P.; Mukai, K.; Takeda, Y.; Matsumoto, T.; Matsumura. K.; Takakura, M.; Arai, H.; Taguchi, T.; Maenosono, S. *ACS Omega* **2017**, *2*, 4929–4937.
(48) López-Ortega, A.; Takahashi, M.; Maenosono, S.; Vavassori, P. *Nanoscale* **2018**, *10*, 18672–18679.
(49) Kobayashi, S.; Kojidani, T.; Osakada, H.; Yamamoto, A.; Yoshimori, T.; Hiraoka, Y.; Haraguchi, T. *Autophagy* **2010**, *6*, 36–45.
(50) Fujita, N.; Morita, E.; Itoh, T.; Tanaka, A.; Nakaoka, M.; Osada, Y.; Umemoto, T.; Saitoh, T.; Nakatogawa, H.; Kobayashi, S.; Haraguchi, T.; Guan, J.-L.; Iwai, K.; Tokunaga, F.; Saito, K.; Ishibashi, K.; Akira, S.; Fukuda, M.; Noda, T.; Yoshimori, T. *J. Cell. Biol.* **2013**, *203*, 115–128.

## Silver Salts

| Name | Composition; | Form; | Purity | Cat. No. |
|---|---|---|---|---|
| Silver chloride | AgCl | powder and chunks | 99.999% trace metals basis | **204382-1G**<br>**204382-5G**<br>**204382-25G** |
| | AgCl | beads | 99.998% trace metals basis | **449571-1G**<br>**449571-5G** |
| Silver cyanide | AgCN | powder | 99.96% trace metals basis | **438421-5G**<br>**438421-25G** |
| Silver iodide | AgI | powder and chunks | 99.999% trace metals basis | **204404-10G** |
| | AgI | powder | 99% | **226823-25G**<br>**226823-100G** |
| Silver nitrate | $AgNO_3$ | solid<br>crystalline | 99.9999% trace metals basis | **204390-1G**<br>**204390-10G**<br>**204390-50G**<br>**204390-250G**<br>**204390-2KG** |
| | $AgNO_3$ | solid<br>powder | ≥99.999% trace metals basis | **792276-10G** |
| Silver nitrite | $AgNO_2$ | powder | 99.98% trace metals basis | **545015-5G**<br>**545015-25G** |
| | $AgNO_2$ | powder | 99% | **227188-10G**<br>**227188-50G** |
| Silver perchlorate | $AgClO_4$ | solid | 97% | **674583-5G**<br>**674583-25G** |
| Silver perchlorate monohydrate | $AgClO_4 \cdot H_2O$ | crystalline | 99.999% trace metals basis | **379778-5G**<br>**379778-25G** |
| Silver perchlorate hydrate | $AgClO_4 \cdot xH_2O$ | powder or crystals | ≥96.0%, AT | **85271-10G** |
| | $AgClO_4 \cdot xH_2O$ | crystalline | 99% | **226548-5G**<br>**226548-25G** |

## Cobalt Precursors

| Name | Composition; | Form; | Purity | Cat. No. |
|---|---|---|---|---|
| Cobalt(II) acetate | $(CH_3CO_2)_2Co$ | crystals and lumps | 99.99% trace metals basis | **399973-1G**<br>**399973-10G** |
| Cobalt(II) acetylacetonate | $Co(C_5H_7O_2)_2$ | powder and chunks | 97% | **227129-50G**<br>**227129-250G** |
| Cobalt(III) acetylacetonate | $Co(C_5H_7O_2)_3$ | granular<br>powder or crystals | 99.99% trace metals basis | **494534-5G**<br>**494534-25G** |
| Cobalt(II) chloride | $CoCl_2$ | beads | 99.999% trace metals basis | **409332-1G**<br>**409332-5G** |
| | $CoCl_2$ | beads | 99.9% trace metals basis | **449776-5G**<br>**449776-25G** |
| | $CoCl_2$ | powder | 97% | **232696-5G**<br>**232696-100G**<br>**232696-500G** |
| Cobalt(II) chloride hexahydrate | $CoCl_2 \cdot 6H_2O$ | - | 97.0-102.0%, KT w≥97% | **769495-100G** |
| Cobalt(II) chloride hydrate | $CoCl_2 \cdot xH_2O$ | powder and chunks | 99.999% trace metals basis | **203084-10G** |
| Cobalt(II) hydroxide | $Co(OH)_2$ | powder | 95% | **342440-250G** |
| Cobalt(II) acetate tetrahydrate | $(CH_3COO)_2Co \cdot 4H_2O$ | powder and chunks | 99.999% trace metals basis | **437875-1G**<br>**437875-10G** |

## Poly(L-lysine)

| Name | Molecular Weight | Cat. No. |
|---|---|---|
| Poly-L-lysine hydrobromide | - | **L8295-5G** |
| | 1,000-5,000 | **P0879-25MG**<br>**P0879-100MG**<br>**P0879-500MG**<br>**P0879-1G** |
| | ≤15,000 by MALLS<br>4,000-15,000 by viscosity | **P6516-25MG**<br>**P6516-100MG**<br>**P6516-500MG**<br>**P6516-1G** |
| | 15,000-30,000 by viscosity | **P7890-25MG**<br>**P7890-100MG**<br>**P7890-500MG**<br>**P7890-1G** |
| | 30,000-70,000 | **P2636-25MG**<br>**P2636-100MG**<br>**P2636-500MG**<br>**P2636-1G** |
| | 70,000-150,000 by viscosity | **P1274-25MG**<br>**P1274-100MG**<br>**P1274-500MG**<br>**P1274-1G** |
| | 150,000-300,000 | **P1399-25MG**<br>**P1399-100MG**<br>**P1399-500MG**<br>**P1399-1G** |
| | ≥300,000 | **P1524-25MG**<br>**P1524-100MG**<br>**P1524-500MG**<br>**P1524-1G** |

## Fluorescent Iron Oxide Nanoparticles

| Name | Fluorescence Emission (nm) | Concentration | Cat. No. |
|---|---|---|---|
| Iron oxide incorporated conjugated polymer nanoparticles | $\lambda_{em}$ = 475 | 100 µg/mL in $H_2O$ | **905054-250UL** |
| | $\lambda_{em}$ = 510 | 100 µg/mL in $H_2O$ | **905038-250UL** |
| | $\lambda_{em}$ = 550 | 100 µg/mL in $H_2O$ | **905046-250UL** |
| | $\lambda_{em}$ = 680 | 100 µg/mL in $H_2O$ | **904996-250UL** |

## Silver Nanoparticles

| Description, | Concentration | Dimension | Cat. No. |
|---|---|---|---|
| - | 0.02 mg/mL in aqueous buffer | particle size 10 nm (TEM) | **730785-25ML** |
| | 0.02 mg/mL in aqueous buffer | particle size 20 nm (TEM) | **730793-25ML** |
| | 0.02 mg/mL in aqueous buffer | particle size 40 nm (TEM) | **730807-25ML** |
| | 0.02 mg/mL in aqueous buffer | particle size 60 nm (TEM) | **730815-25ML** |
| | 0.02 mg/mL in aqueous buffer | particle size 100 nm (TEM) | **730777-25ML** |
| $\lambda_{max}$ 480 nm | 0.02 mg/mL in water | avg. part. size 100 nm | **796018-25ML** |
| $\lambda_{max}$ 390 nm | 0.02 mg/mL in water | avg. part. size 10 nm | **795925-25ML** |
| $\lambda_{max}$ 395 nm | 0.02 mg/mL in water | avg. part. size 20 nm | **795933-25ML** |
| PVP functionalized, $\lambda_{max}$ 400 nm | 0.02 mg/mL in water | avg. part. size 30 nm | **795941-25ML** |
| PVP functionalized, $\lambda_{max}$ 425 nm | 0.02 mg/mL in water | avg. part. size 50 nm | **795976-25ML** |
| PVP functionalized, $\lambda_{max}$ 430 nm | 0.02 mg/mL in water | avg. part. size 60 nm | **795984-25ML** |
| PVP functionalized, $\lambda_{max}$ 460 nm | 0.02 mg/mL in water | avg. part. size 80 nm | **795992-25ML** |
| PVP functionalized, $\lambda_{max}$ 485 nm | 0.02 mg/mL in water | avg. part. size 200 nm | **796026-25ML** |
| $\lambda_{max}$ 400 nm | 0.02 mg/mL (in 2mM aqueous sodium citrate) | avg. part. size 30 nm | **796123-25ML** |
| $\lambda_{max}$ 420 nm | 0.02 mg/mL (in 2mM aqueous sodium citrate) | avg. part. size 50 nm | **796131-25ML** |
| $\lambda_{max}$ 455 nm | 0.02 mg/mL (in 2mM aqueous sodium citrate) | avg. part. size 80 nm | **796158-25ML** |
| $\lambda_{max}$ 485 nm | 0.02 mg/mL (in 2mM aqueous sodium citrate) | avg. part. size 200 nm | **796166-25ML** |
| $\lambda_{max}$ 410 nm | 0.02 mg/mL in water | avg. part. size 30 nm | **796190-25ML** |
| $\lambda_{max}$ 415 nm | 0.02 mg/mL in water | avg. part. size 40 nm | **796204-25ML** |
| $\lambda_{max}$ 420 nm | 0.02 mg/mL in water | avg. part. size 50 nm | **796212-25ML** |
| $\lambda_{max}$ 430 nm | 0.02 mg/mL in water | avg. part. size 60 nm | **796220-25ML** |
| $\lambda_{max}$ 470 nm | 0.02 mg/mL in water | avg. part. size 80 nm | **796239-25ML** |

| Description, | Concentration | Dimension | Cat. No. |
|---|---|---|---|
| $\lambda_{max}$ 485 nm | 0.02 mg/mL in water | avg. part. size 100 nm | **796247-25ML** |
| $\lambda_{max}$ 490 nm | 0.02 mg/mL in water | avg. part. size 200 nm | **796255-25ML** |
| $\lambda_{max}$ 410 nm | 0.02 mg/mL in water | avg. part. size 40 nm | **796301-25ML** |
| $\lambda_{max}$ 420 nm | 0.02 mg/mL in water | avg. part. size 50 nm | **796328-25ML** |
| $\lambda_{max}$ 430 nm | 0.02 mg/mL in water | avg. part. size 60 nm | **796336-25ML** |
| $\lambda_{max}$ 470 nm | 0.02 mg/mL in water | avg. part. size 80 nm | **796344-25ML** |
| $\lambda_{max}$ 485 nm | 0.02 mg/mL in water | avg. part. size 100 nm | **796352-25ML** |
| $\lambda_{max}$ 500 nm | 0.02 mg/mL in water | avg. part. size 200 nm | **796360-25ML** |
| $\lambda_{max}$ 415 nm | 0.02 mg/mL in water | avg. part. size 40 nm | **796409-25ML** |
| $\lambda_{max}$ 425 nm | 0.02 mg/mL in water | avg. part. size 50 nm | **796417-25ML** |
| $\lambda_{max}$ 435 nm | 0.02 mg/mL in water | avg. part. size 60 nm | **796425-25ML** |
| $\lambda_{max}$ 470 nm | 0.02 mg/mL in water | avg. part. size 80 nm | **796433-25ML** |
| $\lambda_{max}$ 495 nm | 0.02 mg/mL in water | avg. part. size 100 nm | **796441-25ML** |
| $\lambda_{max}$ 500 nm | 0.02 mg/mL in water | avg. part. size 200 nm | **796468-25ML** |

## Silver Nanoplates

| Functional Group | Absorption | Concentration (mg/mL) | Cat. No. |
|---|---|---|---|
| PVP | 550 nm | ~ 1 (in water with 5 mM sodium borate buffer) | **807532-1ML** |
| | 650 nm | ~ 1 (in water with 5 mM sodium borate buffer) | **807524-1ML** |
| | 750 nm | ~ 1 (in water with 5 mM sodium borate buffer) | **807516-1ML** |
| | 850 nm | ~ 1 (in water with 5 mM sodium borate buffer) | **807699-1ML** |
| | 950 nm | ~ 1 (in water with 5 mM sodium borate buffer) | **807680-1ML** |
| | 1050 nm | ~ 1 (in water with 5 mM sodium borate buffer) | **807672-1ML** |
| | 550 nm | 0.02 (in water with 5 mM sodium borate buffer) | **796476-25ML** |
| | 650 nm | 0.02 (in water with 5 mM sodium borate buffer) | **796484-25ML** |
| | 750 nm | 0.02 (in water with 5 mM sodium borate buffer) | **796492-25ML** |
| | 850 nm | 0.02 (in water with 5 mM sodium borate buffer) | **796506-25ML** |
| | 950 nm | 0.02 (in water with 5 mM sodium borate buffer) | **796514-25ML** |

Merck KGaA
Frankfurter Strasse 250
64293 Darmstadt, Germany



Lit. No. MK_BR4819EN
2019-25588